UNIVERSITY OF OKLAHOMA

GRADUATE COLLEGE

RADIATION-INDUCED ACOUSTIC IMAGING SYSTEM DEVELOPMENT AND APPLICATIONS

A THESIS

SUBMITTED TO THE GRADUATE FACULTY

in partial fulfillment of the requirements for the

Degree of

MASTER OF SCIENCE

By

SIQI WANG
Norman, Oklahoma
2019

RADIATION-INDUCED ACOUSTIC IMAGING SYSTEM DEVELOPMENT AND APPLICATIONS

A THESIS APPROVED FOR THE
SCHOOL OF ELECTRICAL AND COMPUTER ENGINEERING

BY

Dr. Liangzhong Xiang, Chair

Dr. Yingtao Liu

Dr. Bin Zheng

Acknowledgements

Firstly, I would like to express my gratitude to my supervisor Dr. Xiang, Liangzhong for the useful comments, remarks and encouragement through the learning process of this master thesis.

Secondly, I would like to thank Dr. Liu, Yingtao for his help and support throughout the collaboration on pNDT system development project.

I would also like to thank my other committee member Dr. Zheng, Bin for serving as my committee member and providing me useful feedback.

Furthermore, I would like to thank all my past and present lab colleagues for their contribution and collaboration.

This thesis would not have been possible without the support of anyone mentioned above.

Table of Contents

List of Figures

Abstract

This thesis reports the development of three different radiation induced acoustic imaging systems excited by a pulsed laser, X-ray, and electric field respectively. Firstly, a laser induced photoacoustic imaging system for non-destructive testing (pNDT) is presented in Chapter I. The pNDT is comprised of three major components: picosecond pulsed laser based ultrasonic actuator, ultrasound receiver, data processing and computing subsystem. A CFRP composted was scanned and both the micro-scale and macro-scale damage are detected and localized with spatial resolution of 100 μm. Secondly, an X-ray-induced acoustic tomography (XACT) system was developed for bone imaging in Chapter II. A 500 KHz ultrasound transducer was used to obtain a 3D image of a chicken bone placed underneath the -ray source. The first XACT biological bone sample was linearly scanned with 12-posiiton increments. The image was then obtained with a back-projection reconstruction algorithm. The chicken bone was successfully reconstructed, demonstrating the potentials of XACT systems in bone density *in vivo imaging.* Thirdly, a new imaging modality, electroacoustic tomography (EAT), was designed for electrical therapy monitoring. The acoustic signals generated by high-voltage pulsing electrical fields during electrical therapies were detected and analyzed. The optimal parameters for effective EA signal generation were found. The results demonstrated the potentials of the pNDT system in ultra-high resolution CFRP NDT, the XACT system in fast 3D bone imaging, and the EAT system in real-time electric therapy monitoring.

Chapter 1: Introduction

1.1 Radiation-induced Acoustic Wave

1.1.1 The Discovery of Radiation-induced Acoustic Wave

In 1880, Alexander Graham Bell discovered that substances emit sound when a 'vibratory beam of light' falls upon them [1]. This discovery marked the first time that a radiation-induced acoustic wave was discovered, in the form of light-induced photoacoustic (PA) wave. It would not be until around 100 years after the discovery of photoacoustic effect, with the advancement of ultrasound transducers and computers, PA phenomenon began to be heavily investigated by scientists for biomedical purposes [2]–[4].

Inspired by the discovery of PA waves, scientists started the investigations of generating acoustic waves with other types of radiation excitation sources. In 1980, Theodore Bowen proposed the theory that all non-ionizing radiation which deposit heat in short pulses should be able to produce acoustic waves, and such waves are named thermoacoustic (TA) waves [5]. A few years later, X-ray-induced acoustic (XA) waves were discovered in 1983 by Wolfgang Sachse, expanding the possible acoustic wave generating excitation sources to ionizing radiations. Recently, electroacoustic (EA) waves were also generated and detected with a nanosecond electric pulse excitation source [6].

1.1.2 The Generation and Propagation of Radiation-induced Acoustic Wave

The fundamental principle of radiation-induced acoustic wave generation includes 3 steps: (1) the target medium absorbs radiation energy from the excitation source; (2) the absorbed radiation energy is converted into heat and generates a localized

temperature rise; (3) the temperature rise causes thermoelastic expansions in the medium, which result in the generation of acoustic waves [4], [7], [8].

The efficient generation of radiation-induced acoustic waves requires the satisfaction of two conditions, the thermal and stress confinements [9]. The thermal confinement indicates that the thermal diffusion during radiation excitation can only be neglected if the pulse with τ of the excitation source is smaller than the target medium's relaxation time τ_{th} [7], [8], i.e.,

$$\tau < \tau_{th} = \frac{d_c^2}{4D_T}. \quad (1)$$

In this equation, d_c represents the desired spatial resolution, and D_T indicates the thermal diffusivity of the target medium.

The stress confinement means the volume expansion of the absorber during the excitation period can only be neglected if the pulse width of the radiation source is smaller than the stress exit time of the target medium [7], [8]. The condition is described as follows:

$$\tau < \tau_{st} = \frac{d_c^2}{v_s}, \quad (2)$$

where v_s is the speed of sound in the target medium.

Once the thermal diffusion and the medium volume expansion can be mathematically neglected, the initial local pressure rise $p_0(r)$ caused by the radiation energy absorption can be modelled with the following equation[4], [8]:

$$p_0(r) = -\frac{\beta}{c}\frac{\partial}{\partial_t}H(r,t). \quad (3)$$

In equation (3), β and c represent the target medium related thermal coefficient constant of volume expansion and heat capacity constant respectively. $H(r,t)$ indicates the

heating function, which is specific to excitation sources and targets, defined as thermal energy converted per unit volume and time, resulted from the radiation energy absorption. The first time derivative of $H(r,t)$ is the resulted heating from energy absorption. The initial local pressure$p_0(r)$ is directly proportional to the spatial distribution of the heat function $H(r,t)$.

The general radiation-induced acoustic wave generation and propagation equation (equation 4) in an inviscid medium can be obtained by implementing equation (3):

$$\nabla^2 p(r,t) - \frac{1}{c^2}\frac{\partial^2}{\partial_t{}^2} p(r,t) = -\frac{\beta}{C}\frac{\partial}{\partial_t} H(r,t), \qquad (4)$$

where $p(r,t)$ denotes the acoustic pressure at location r and time t.

The detection of radiation-induced acoustic pressure generated by an arbitrarily heterogeneous medium can be solved by applying three-dimensional Green's function [10], [11]. The radiation-induced acoustic signal $p(\boldsymbol{r},\boldsymbol{t})$ picked up by an ultrasound transducer is given as follows [12]:

$$p(\boldsymbol{r},\boldsymbol{t}) = \frac{1}{4\pi {C_p}^2}\frac{\partial}{\partial_t}\int dr' \frac{1}{|\boldsymbol{r}-r'|} H(\boldsymbol{r},\boldsymbol{t}-t')\Big|_{t'=\frac{r-r'}{v_s}}, \qquad (5)$$

where r' and t' denotes the excitation location and time, respectively. C_p is the specific heat capacity at constant pressure. Equation (5) can be used to calculate radiation-induced acoustic wave generated on an arbitrarily heterogenous radiation absorbing object.

1.2 Radiation-induced Acoustic Imaging and Its Application in Biomedicine

1.2.1 Medical Imaging

Since the X-ray was discovered more than one hundred years ago, radiation based X-ray imaging has been invaluable in medical diagnosis, prevention and treatment planning

[13]–[16]. Among all the radiation based imaging techniques, X-ray computed tomography (CT) demonstrated great utility in providing high-resolution, three-dimensional, and non-invasive medical imaging method since its invention in 1970s. However, CT based imaging techniques require a large amount of projection data. Long scanning time and high radiation dose are required to achieve adequate imaging results. Over 29,000 future cancers are estimated to be related to CT scans performed in the United States in 2007 alone [17]. The radiation-induced acoustic imaging method known as X-ray acoustic computed tomography (XACT) was introduced and demonstrated as a novel medical imaging modality in 2013 by Xiang, etc. [18]. XACT not only takes the advantage of high-contrast and specificity characteristics from its radiation source, but also inherits the high spatial resolution from the ultrasound transducer. In contrast to the long radiation exposure time require for CT techniques because the generated acoustic waves propagate spherically from the excitation point. The XACT imaging system only needs a single X-ray projection to achieve a high-resolution 3D reconstruction. Thus, the total radiation dose can, theoretically, be drastically reduced with XACT imaging.

Since the introduction of XACT, new biomedicine applications and different configurations have been studied by research groups around the world [19]–[21]. The latest development of XACT imaging systems utilizes a ring ultrasound-transducer array to achieve fast and high resolution 2D reconstruction. A schematic of the system setup is demonstrated in Figure 1 [22]. In this setup of XACT system, the generated acoustic signals are acquired by the 128 ultrasound transducer elements on the ring array. The imaged sample is placed in the center of the ring array. Figure 2 shows an OU logo sample

reconstruction obtained from such setup [22]. The result yielded a spatial resolution of 138 μm, from the 5 MHz transducer array.

Although XACT system experiments on simple lead sample yielded great results, challenges remain for it to acquire high signal-to-noise ratio (SNR) acoustic signals from less X-ray absorbing objects. Prior to this thesis, complex biological samples have never been imaged with XACT systems.

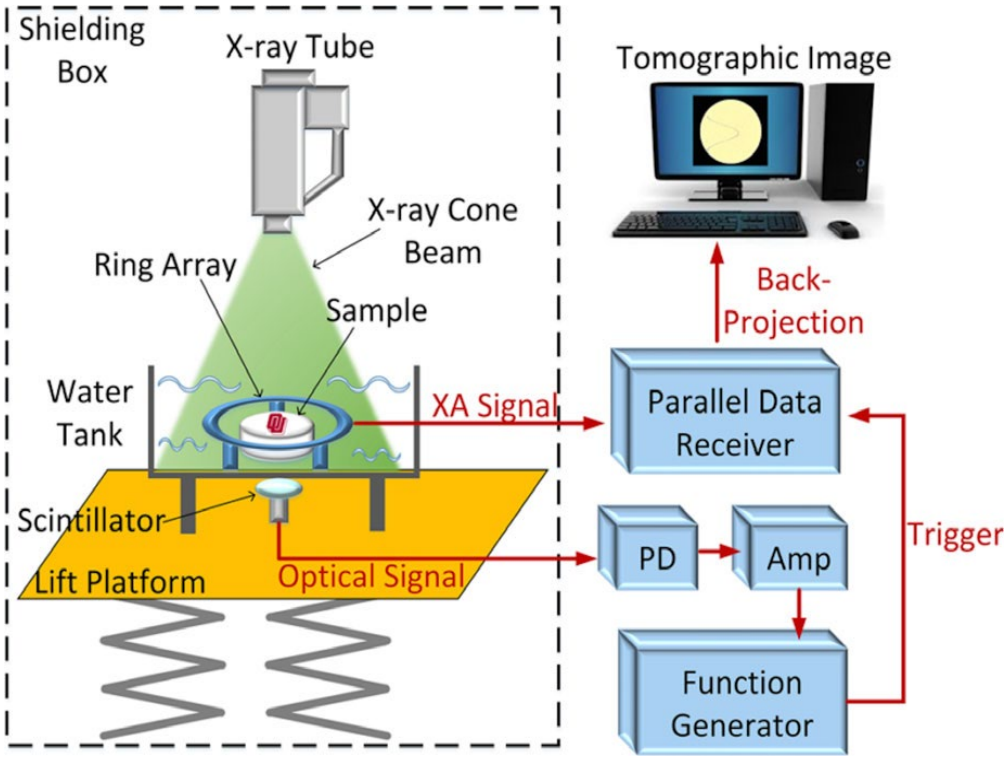

Figure 1. Schematic of the ring array implemented XACT system

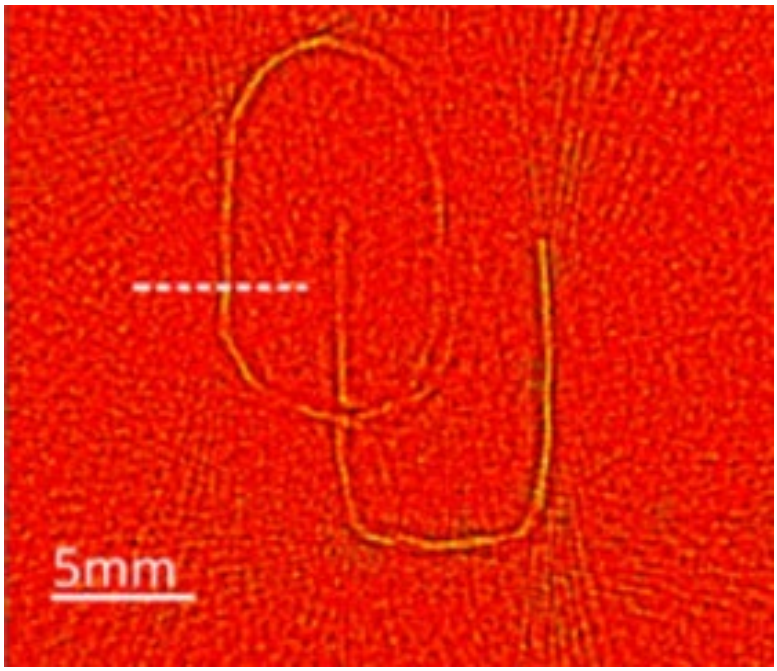

Figure 2. OU logo sample reconstruction. The original sample is made of 150 μm lead sheets

1.2.2 Dosimetry for Radiation Therapy

Radiation therapy (also known as radiotherapy) is a cancer treatment that uses a localized high-energy beam of ionizing radiation to kill or slow the growth of cancerous cells [23]. However, during the radiation procedure the high-energy radiation can also damage the health of surrounding tissues. Therefore, maximizing the radiation damage on cancer cells while maintaining a minimum amount of dose to healthy cells is the most important principle in radiation therapy. *In vivo* radiation therapy dosimetry was created to ensure that radiation therapy treatment is being delivered with the best efficiency by measuring the radiation dose absorbed on an object [24]. Many national and international institutions recommend *in vivo* radiation therapy dosimetry as a safety tool to avoid major operation errors.

Currently, the most established clinical dosimetry techniques include ion chambers (ICs), chemiluminescent dosimeters (TLDs), and optically stimulated luminescent dosimeters (OSLDs). However, all of the mentioned techniques are limited in terms of operation time or ease of implementation [25]. The basic mechanism of radiation-induced acoustic imaging is based on the radiation energy absorbed by target mediums. Naturally, Radiation-induced acoustic imaging systems have the potential to be an effective tool for non-invasive *in vivo* dosimetry during radiation therapies.

X-ray-induced acoustic (XA) imaging utilizes acoustic waves to determine the energy absorption from X-ray photons. Simulations to demonstrate XA imaging's feasibility of being implemented as a dosimetry method in X-ray radiation therapies have already been demonstrated by researchers [26]. Experimental X-ray-induced acoustic computed

tomography (XACT) results have also been obtained and analyzed with theoretical models [27]. All the research results obtained so far indicate that XA imaging has tremendous potential to be a useful and effective *in vivo* X-ray dosimeter in the clinics.

In addition, this study introduces a new radiation-induced acoustic imaging technique, electroacoustic (EA) imaging, that will be used as a new electric therapy monitoring method. The experimental results will be demonstrated to showcase the feasibility of such technique in measuring the electric field intensity.

1.3 Radiation-induced Acoustic Imaging and Its Application in NDT

Non-destructive Testing (NDT) describes the technology of evaluating a material, component or system without damaging the integrity of the article itself [28]. Because NDT does not leave permanent alterations on the object examined, the techniques are high valuable in many fields including manufacturing, healthcare and art, etc. [29], [30]. Today's NDT field includes a great variety of methods. The predominating techniques include various acoustic testing configurations, radiographic testing systems and electrical impedance tomography [31], [32]. However, these methods all come with certain limitations. For example, acoustic testing methods require high frequency ultrasound transducers to provide high resolution spatial information; although, with high frequency ultrasound receivers, the imaging depth of the acoustic system will be limited to a relatively low value. Conventional radiographic testing systems either require a long operation time, like Computerized Tomography, or has limited accessibilities such as X-ray systems [31].

Radiation-induced acoustic techniques can shorten the distance that the acoustic wave needs to travel in the signal attenuating medium, which can theoretically provide double the penetration power of conventional acoustic testing methods. In terms of accessibility, both the receiving and transmitting ends of the radiation-induced acoustic NDT systems can be positioned on the same side of the testing object, which does not have the space limitation of transmission based radiographic testing systems. Since the radiation-induced acoustic waves propagate spherically in a three-dimensional (3D) space, a complete 3D reconstruction could theoretically be obtained from a single projection of radiation. Thus, the total radiation time can be reduced drastically when compared to conventional radiographic methods.

Recently, a simulation study of an XACT system for concrete infrastructures NDT has been performed [33]. Figure 3 shows the imaging schematic of the proposed XACT concrete inspection system. Different from conventional X-ray computed tomography, the XACT system only needs one side of the inspecting target for operation. In this simulation study, both the large-scale and sub-millimeter-scale of the concrete structure XACT reconstructions have been separately demonstrated [33]. The macro-scale reconstruction of a 1 m diameter concrete beam is shown in Figure 4. The macro-level XACT reconstruction was clearly able to resolve the embedded defect at the level of the white dashed line. The micro-scale that defects resolving power of the XACT system is demonstrated with a model of a 30 cm concrete beam with embedded rebars. Figure 5a shows the XACT reconstruction of the rebar-embedded concrete beam model. By subtracting a health rebar embedment image off the reconstructed image, the defects surrounding the rebar were able to be identified in Figure 5b [33].

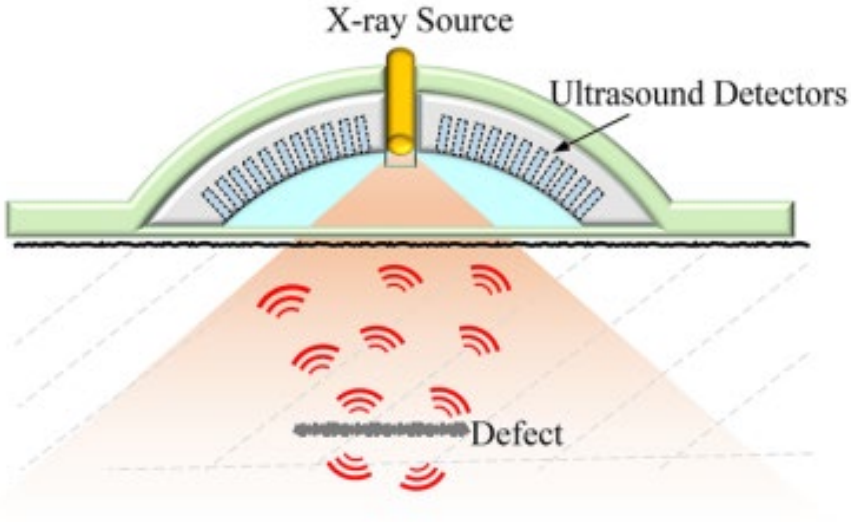

Figure 3. The schematic diagram of the concrete infrastructure inspecting XACT system

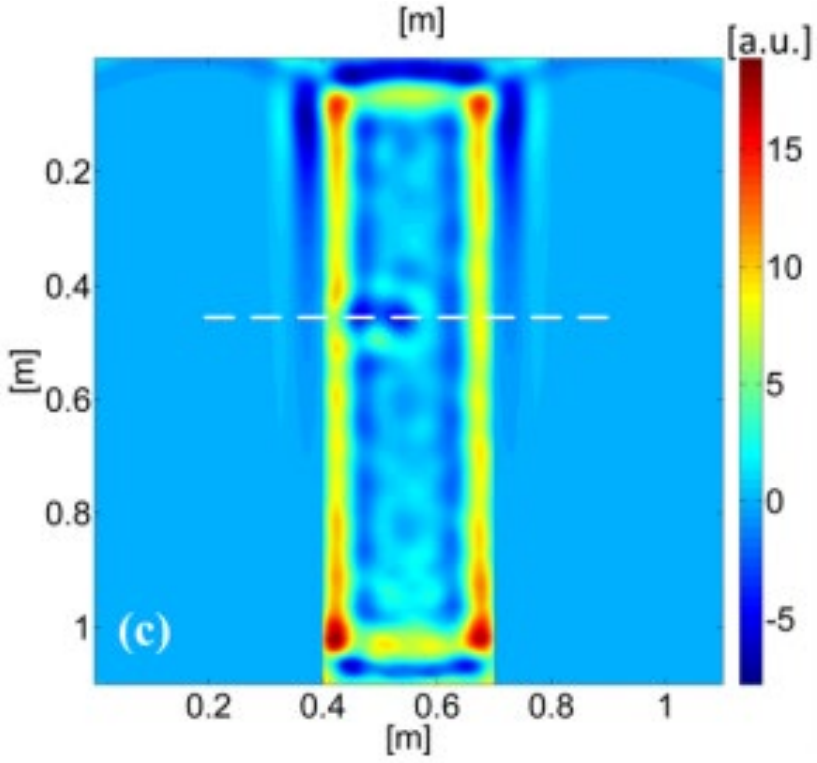

Figure 4. The XACT reconstruction of a 1m diameter concrete beam

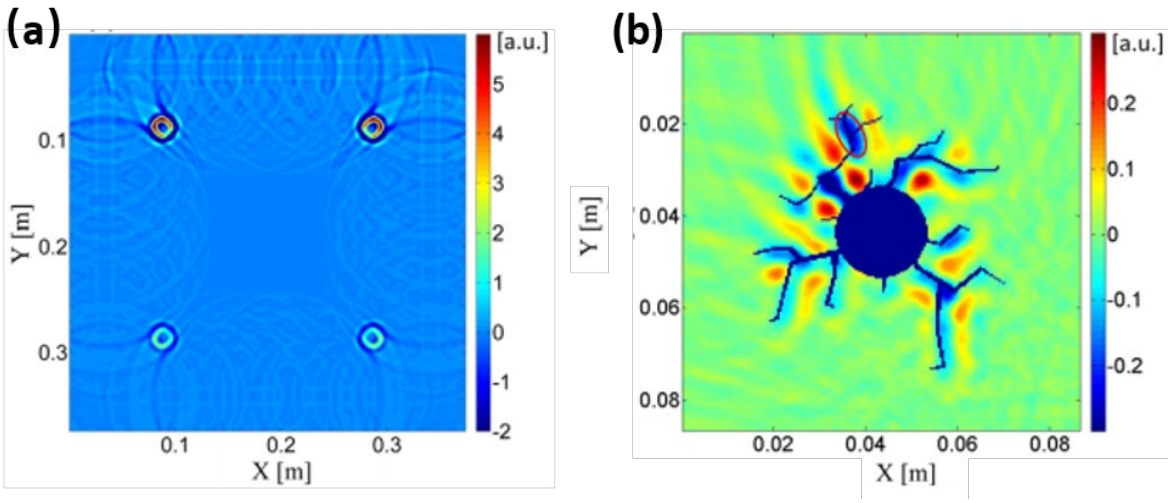

Figure 5. The XACT reconstruction the cross section of a 30 cm rebar-embedded concrete beam (a) the XACT reconstruction of the rebar-embedded concrete beam model (b) the defects surrounding the rebar after the health rebar subtraction

The simulation studies of XACT systems show promising potential of such techniques to be implemented in structure NDT. However, these simulation results still need experimental verification. Besides utilizing X-ray-induced acoustic waves, a thin 3D composite NDT system, based on photoacoustic imaging, was proposed by Matthew O'Donnell, etc. in 2016 [34]. The study showed great potential of the photoacoustic imaging based method in NDT. In this thesis, the photoacoustic imaging method will be further explored along with a demonstration of a high-resolution 3D NDT system in the following chapter.

1.4 Objectives of This Study

In this study, a high-resolution photoacoustic microscopy non-destructive testing (pNDT) system for the detection of damage precursors in carbon fiber reinforced plastic

(CFRP) composites has been developed. The developed pNDT system consists of four major parts: a high-precision, down to 100 nm resolution, 2-axis scanning stage controlled by NI LabVIEW software [35], a picosecond pulsed laser radiation source, a high frequency ultrasound receiver, and the data acquisition, processing and reconstructing subsystem. The system configuration, control and data acquisition are presented in detail. The 3D microstructure of the structural grid within the CFRP composite has been reconstructed with addition analysis.

Additionally, an X-ray-induced acoustic computed tomography (XACT) system for bone imaging has been developed. The system for bone imaging utilizes a miniature short-pulsed X-ray generator, an ultrasound transducer, a manual linear positioning stage, and data acquisition and process subsystem. Acoustic signals were successfully detected and demonstrated with a linearly scanned chicken bone image, marking the first time that XACT reconstructed an image of a biological sample. After the demonstration of the chicken bone reconstruction results, future system upgrade directions will be discussed, along with addition tests on upgrade components.

Finally, an electroacoustic tomography (EAT) system for electrical therapy monitoring was developed in this study. The system configuration, the design of the short-pulse high voltage generating circuit, and the data acquisition process of the EAT system will be explained in Chapter 4. Successfully detected acoustic waves with different voltage electrical fields will be demonstrated and future experimental setups will be discussed.

Chapter 2: Photoacoustic Imaging for NDT

2.1 NDT for CFRP Background

Carbon fiber reinforced polymer (CFRP) composites is a specially manufactured and reinforced material which contains carbon fibers [36]. Due to their outstanding strength-to-weight ratio, thermomechanical properties and superior corrosion resistance compared to traditional material, CFRP composites have been widely used as core structural materials for a wide range of manufacturing fields, including aerospace, automotive, infrastructure, healthcare, etc. [29], [37], [38].

Yet, CFRP composites can still become damaged whether the material is in transit or under service. Typical causes include impact that occurs in a short amount of time and fatigue, which happens over a longer period of time [39]–[41]. Moreover, structural damages, which include microscale damage precursors and macroscale failures, can occur without visible signs on the surface of the material. Common microscale damage precursors include fiber breakages, fiber pullout, and matrix cracks. Delamination has been considered the most common macroscale damage that can result in catastrophic failure in the material structure. Therefore, it is crucial to find an adequate NDT method that is capable of 3D high-resolution and high-accuracy imaging to detect and characterize the damage precursors in CFRP composites [34].

Techniques such as ultrasound imaging, X-ray tomography, and IR thermography are the most common NDT methods used for CFRP materials [42], [43]. All the techniques mentioned exhibit certain limitations and weakness. In conventional ultrasound NDE systems, ultrasound waves are generated in narrow frequency bands and

are only able to detect the internal structure in a relative low resolution. Next, Three-dimensional (3D) X-ray based NDT methods can take an extended period to operate and will need a large space on both receiving and transmitting ends. Lastly, IR thermography does not allow 3D imaging and fails to provide fine microstructural details.

Laser-induced PA imaging techniques have been studied as a plausible alternative to the conventional methods previously stated [44]–[46]. Theoretically, PA imaging provides many advantages over conventional NDT methods, providing much better resolution than ultrasound-based solutions combined with outstanding versatility in one package. The characteristics of PA imaging making it a suitable solution for CFRP composites NDT.

The goal for the developed laser-induced photoacoustic non-destructive testing (pNDT) system is to provide three-dimensional (3D) extra-high-resolution damage precursor detection in CFRP composites. To achieve such goal, a picosecond pulsed laser source and a 20MHz ultrasound transducer were used as the excitation source and receiving end for the system. Details of the system configuration, control, and data acquisition are presented.

2.2 Experimental Setup and Methods

2.2.1 Photoacoustic Imaging theory

The fundamental principles of radiation-induced acoustic imaging were explained in the previous chapter. In light-induced PA imaging, the heating function is given as follows [7]:

$$H(r,t) = \mu_a(r)\phi(r,t), \quad (6)$$

where μ_a represents the light absorption coefficient, the probability of photon absorption per unit path length, of the target medium.

Because μ_a is largely medium specific and wavelength specific, in PA imaging, different wavelengths of light source will excite different types of photo absorbers. In the sense of non-destructive testing, different materials or air gaps will show a different light absorption property. Thus, based on the differences of acoustic signal amplitudes, different materials or air gaps can be shown in the final reconstruction of PA imaging.

2.2.2 pNDT System Configuration

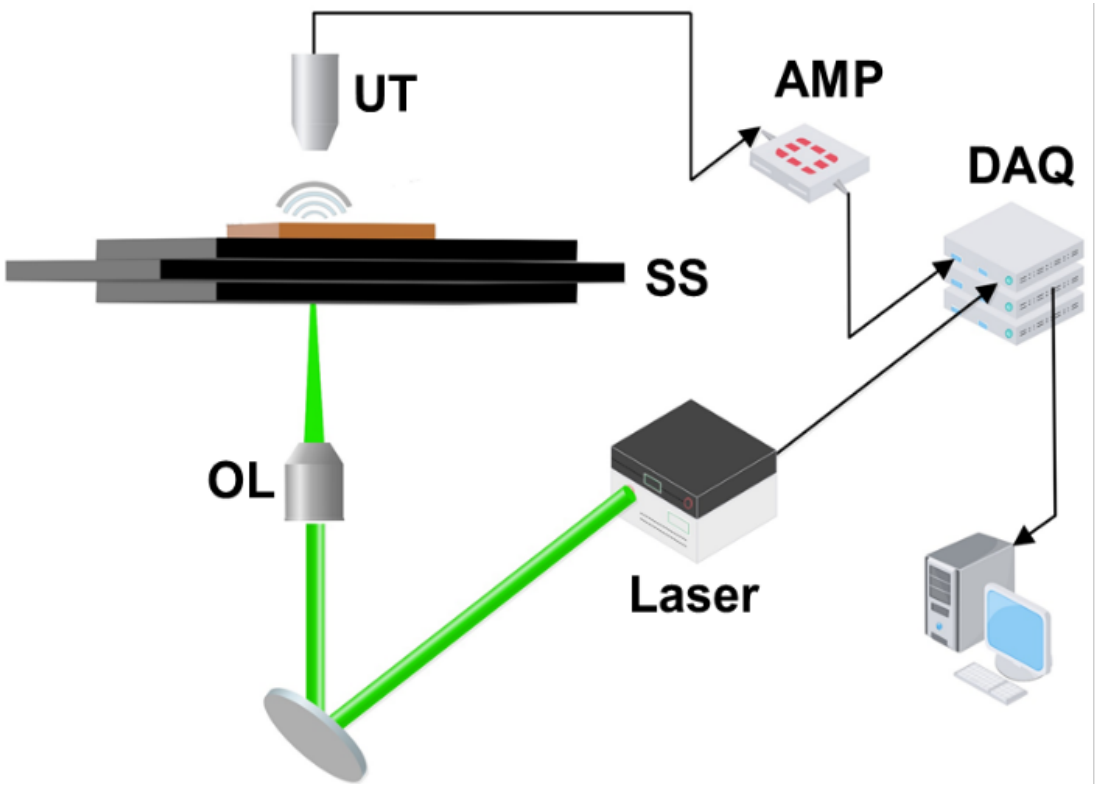

Figure 6. The system diagram of pNDT system. Block-diagram of the pNDT system. UT: Ultrasonic Transducer; SS: Scanning Stage; OL: Objective lens; AMP: Amplifiers; DAQ: Data Acquisition Card; Laser: Green laser (532 nm)

The system diagram of pNDT is shown in **Figure 6**. The pNDT system is comprised of four major components: 1) picosecond pulsed laser (wavelength of 532nm) for the generation of PA waves, 2) Lead zirconate titanate (PZT) piezoelectric ultrasound transducer mounted above the scanning stage, 3) 2-axis high-precision (~100 nm step size) motorized scanning stage fixed between the laser excitation source and the ultrasound transducer and 4) data amplification, acquisition, processing and image reconstruction display. Since sound waves attenuate drastically in air, distilled water was used as a coupling medium between the ultrasound transducer and the CFRP plate. Both the ultrasound transducer and the CFRP plate were immerged in a water tank that was mounted on the top of the scanning stage.

The picosecond laser (COMPILER 532/266, Passat, Ltd., Canada) used in the system can provide an ultrafast laser pulse with pulse width <7 ps. The laser beam was focused by a 0.1 numerical aperture object lens and projected to the bottom surface of the CFRP composite. The pulse repetition rate of the laser is adjustable between 1 Hz and 400 Hz. In the CFRP evaluation experiment, 30 Hz repetition rate was chosen for optimal signal-to-noise ratio while minimizing CFRP surface damage caused by focused high-energy laser beam.

The generated photoacoustic signal was then captured by the PZT ultrasound transducer (U8517149, Olympus NDT) which has a center frequency of 20 MHz, and greater than 50% -6 dB bandwidth. In optical-resolution PA tomography (OR-PAT) systems, the lateral resolution of the system is determined by the focus diameter of the optical source, and the axial resolution of the system is reversely proportional to the bandwidth of the ultrasound transducer. The axial resolution is given by $0.88\, c/\Delta f$, where

c is the speed of sound in the propagation medium, and Δf is the bandwidth of the ultrasonic transducer [4], [47]**.** This 20 MHz center frequency was specifically chosen to provide a theoretical maximum spatial resolution of 132 μm in water, while remaining strong enough penetration power for the acoustic signal to reach to the receiving end. A coaxial low-noise amplifier with a bandwidth of 0.1-1000 MHz at -3 dB and a typical gain of 20 dB (ZFL-1000LN+, Mini-Circuits) received the signals from the transducer and delivered the amplified signals to a secondary amplification stage (ZFL-500+, Mini-Circuits) with a bandwidth of 0.05-500 MHz at -3 dB providing gain of 25 dB. In total, the amplification stage can provide more than 170 gain to the acoustic signal. Amplified signals were recorded by data acquisition card (NI PCI-5153EX, National Instruments). A sampling rate of 500 MHz was used to record 1021 data points at each location. One set of data incorporated 500×500 positions as the scanning stage (LMS203 Fast XY Scanning stage, Thorlabs) moved in the X-Y plane controlled by LABVIEW [35]. Photoacoustic images were reconstructed with two-dimensional back-projection algorithms in MATLAB [48], [49]. An 'X' shaped indent was created with a sharp knife on the top surface of the CFRP plate used in the experiment. A micro-CT of the image is shown in Figure 7 to demonstrate the plate surface and the marking.

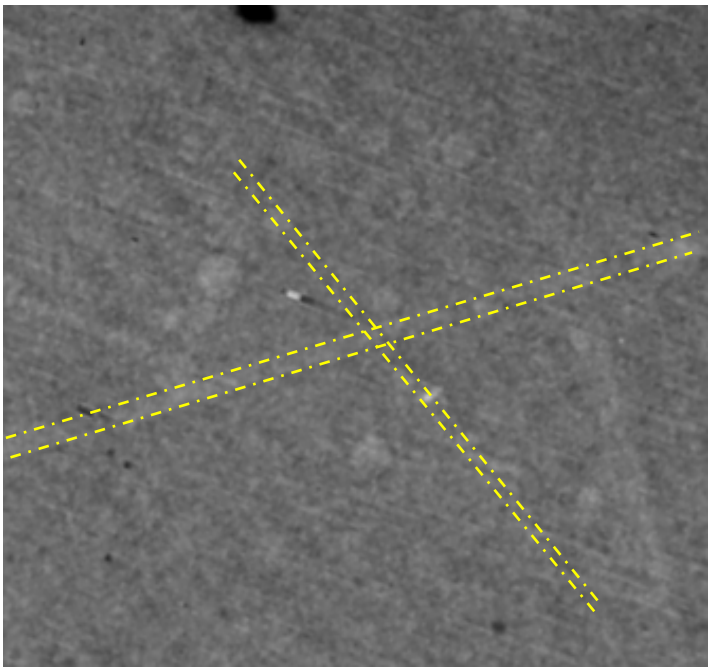

Figure 7. Image of the CFRP plate used in the experiment, the thin indent is marked with yellow dashed lines

2.2.3 Acoustic Signal Attenuation Correction

A typical acoustic wave from the excitation point inside the target medium will travel through different non-ideal propagation mediums and then reach the receiving end of the ultrasound transducer. When sound waves travel through non-ideal propagation mediums, inevitably the attenuation will be going to the amplitude of the acoustic waves. The attenuation of acoustics wave traveling through a heterogenous medium is modeled by Stoke's law given below (equation 6):

$$A(d) = A_0 e^{-\alpha d}, \quad (7)$$

where α, the linear attenuation coefficient of the medium, has a unit of the reciprocal of length, m^{-1}. A_0 denotes the original amplitude of the acoustic wave. After traveling a distance of d in the non-ideal medium, the attenuated amplitude will be A(d).

In this experiment, distilled water was used as a coupling medium between the ultrasound transducer and the scanned CFRP plate. Considering, the attenuation of sound in distilled water is inversely-proportional to the square powered acoustic wave frequency (for 20 MHz, α_{water} = 0.00006325) at room temperature, the sound amplitude loss in water is neglected.

In order to compensate for the ultrasound attenuation in the CFRP material, a time gain correction (TGC) function (equation 7) was applied to all the A-scan signals before the image reconstruction algorithm [34]:

$$A_{TGC}(z_k) = A_0(z_k) \times \exp\big(\alpha(z_k - z_0)\big), \qquad (7)$$

In Equation 7, $A_{TGC}(Z_k)$ denotes the attenuation compensated ultrasound signal at time stamp Z_k. A_0 and α represent the original ultrasound amplitude at the excitation point and the estimated linear attenuation coefficient of CFRP, respectively. The acoustic attenuation compensation correction of a single A-scan is shown in Figure 8.

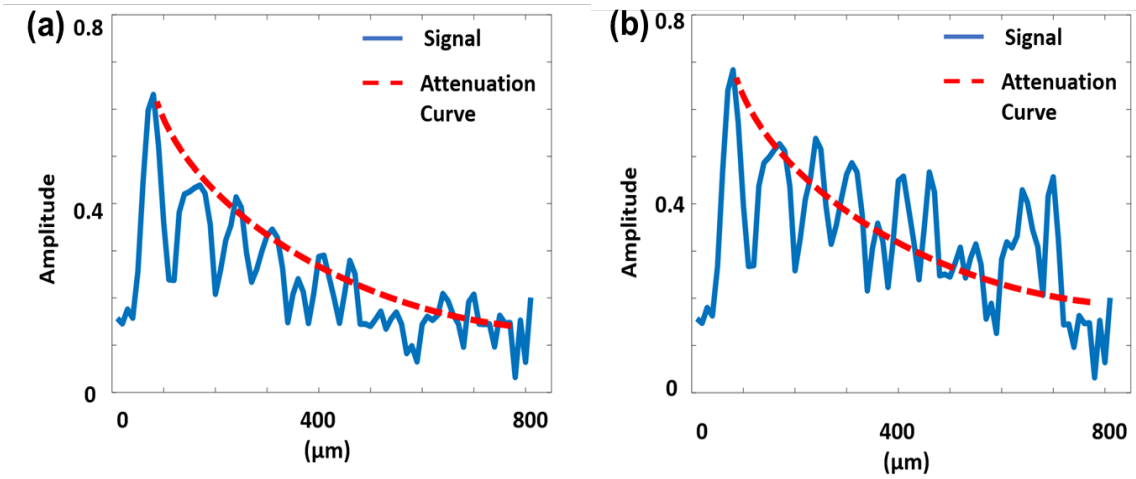

Figure 8. Attenuation Correction (a) Typical full bandwidth photoacoustic A-scan with an assumed signal attenuation function (red dashed curve) and (b) TGC corrected (normalized by the exponent of Equation 7) pNDT A-scan.

2.2.4 LabVIEW Control Program for Stop and Go Scanning

The developed pNDT system uses a stop and go 2D raster scan pattern (Figure 9) [50]. A LabVIEW [35] program was designed to synchronize the 2-axis scanning stage (LMS203 Fast XY Scanning stage, Thorlabs) and the PCI DAQ card (NI PCI-5153EX, National Instruments) for stop and go scanning. The stage will move the CFRP composite by a predefined distance and hold the position until the A-line acoustic signal corresponding to the position is acquired and deposited into a '.txt' file.

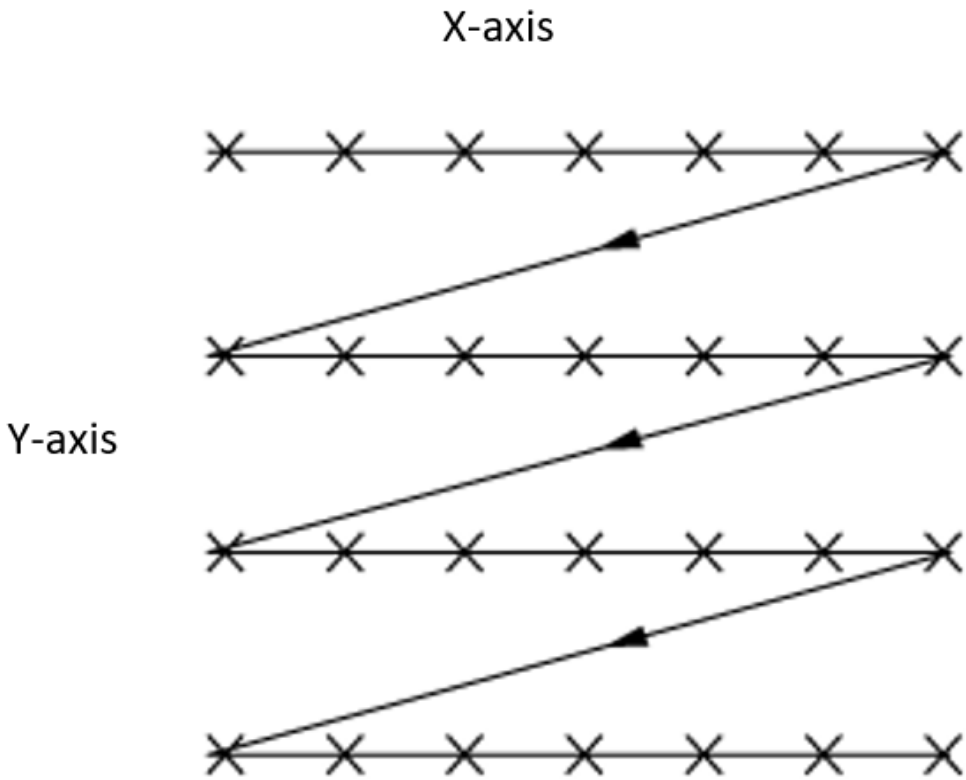

Figure 9. 3D raster scan pattern [50]

The LabVIEW software has two parts. First, the front panel which hosts all the control options and the program diagram where all the graphical logics exist. This part of

the pNDT LabVIEW program can be further divided into two sections: the motor control section and the data acquisition section. Figure 10 demonstrates the motor control section of the LabVIEW front panel design for the pNDT system. On the left side of the motor control section, different setting inputs/outputs are divided and grouped into 3 rectangles. The top rectangle, 'Hardware Setting', houses the initialization settings for the two channel motor controller (BDD202, Thorlabs). The 'Scan Setting' group contains all the input parameters to define the start points, step sizes and number of steps of the scan for each channel, along with calculated scan end points indicators. The last rectangle, 'Scan Iteration', contains two outputs that indicates the position of the scanning stage by showing the horizontal and vertical iterations (steps). In addition to scan parameters, the horizontal and vertical motor drivers (APT, Thorlabs) were installed on the right side of the motor control section of the LabVIEW front panel.

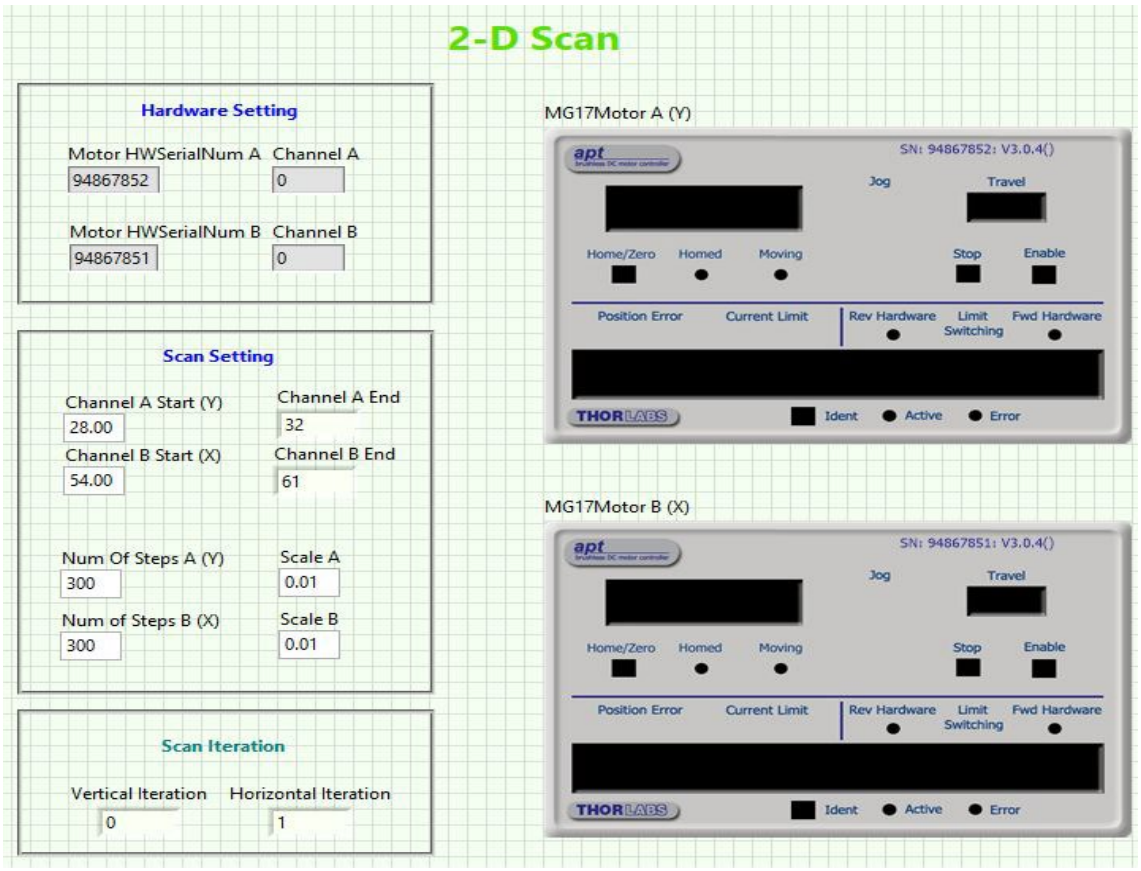

Figure 10. the motor control section of the LabVIEW front panel.

The data acquisition card initialization section of the pNDT program front panel is shown in Figure 11. A scan activation button can be seen between the data acquisition section and the motor initialization section. Additionally, the scan can be further configured with the number of average setting ('Num Avgs') and the step wait time ('ms to wait') for each step. In the pNDT system, two channels of the data acquisition card are used to collect the trigger information from the laser pulsing machine, and the data information from the ultrasound transducer. Inside the data acquisition section on the front panel, the trigger channel and the data channel are grouped separated and labeled as channel 0 and channel 1, which was intended for easier channel recognition on the DAQ card. The horizontal configuration rectangle has input fields to define the minimum

sample rate, minimum record length and the reference position percentage. The reference position setting allows users to define what percentage of the signal acquired will be before the trigger detected. For example, a '0%' setting will set the DAQ card to acquire right at the trigger time point. In addition to input parameters, the horizontal configuration group also houses the actual sampling rate, actual record length and the calculated record duration in seconds. The trigger configuration group can be seen on the right side of the horizontal configuration group. In pNDT system, a DC pulsed signal was sent from the laser machine as the trigger signal.

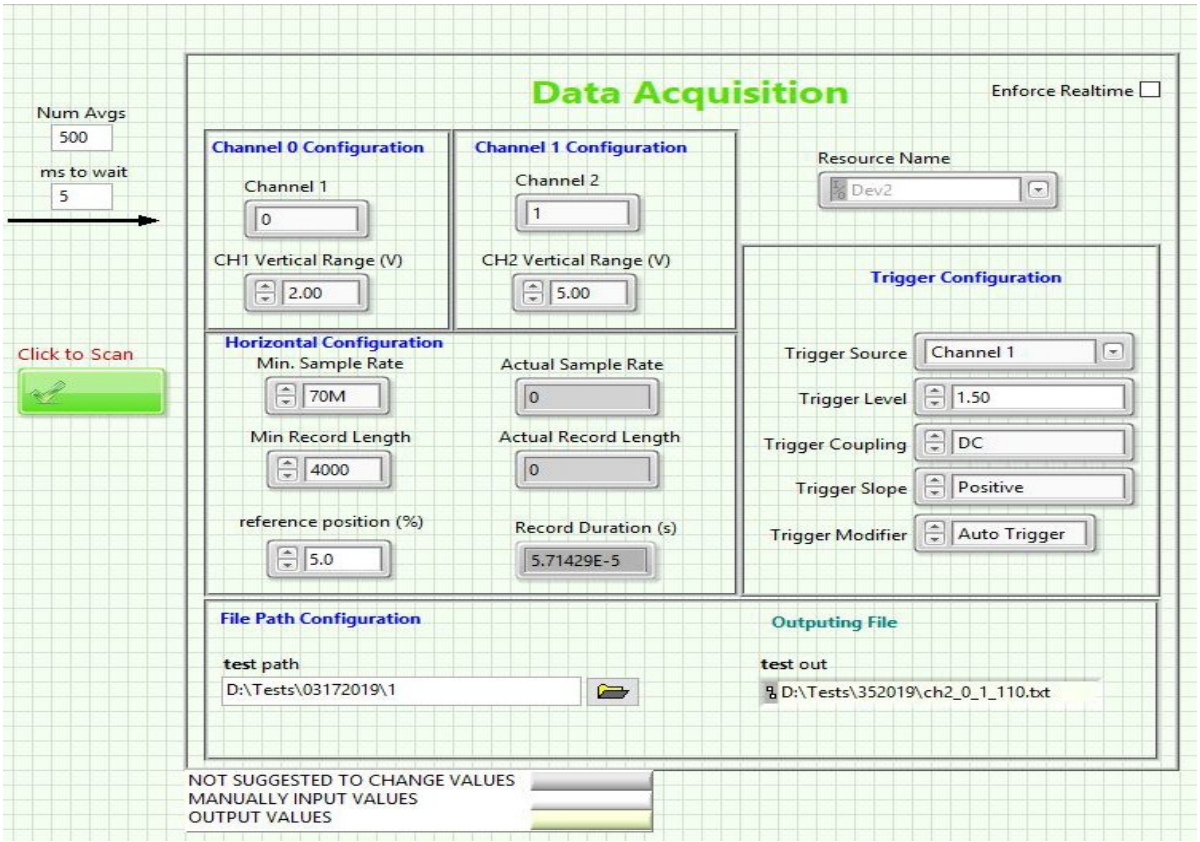

Figure 11. LabVIEW program front panel for pNDT (data acquisition card initialization part)

The logical part of pNDT LabVIEW program can also be divided into two parts: the motor and DAQ card initialization part and the motor movement and data acquisition synchronization part (Figure 12&.13). In the initialization phase of pNDT program diagram, configurations for the DAQ card and the motor are grouped in separate frames. In addition to the configurations, two constantly running while loops are used to perform calculations for the channel end points and the horizontal durations in seconds. The data acquisition synchronization phase of pNDT system LabVIEW program is configured with one stacked sequence structure. The sequence structure contains four sequence frames: motor initialization, motor start, motor operation/data acquisition synchronization and motor/DAQ card stop. The shown image in Figure 13 is the most populated motor operation/data acquisition synchronization frame. The motor operation/data acquisition synchronization frame starts with a while loop with a single switch button. The switch loop is the mechanism of the manual scan start button. Once the scan start button is pressed, the wire information will break out of the while loop, and flow into the next terminals of their paths. After the scan-start switch mechanism, two nested while loops are used to iterate through all the vertical and horizontal positions of the scan. Figure 14 shows a screenshot of the two nested movement-control while loops, when the stack sequence inside of the inner while loop changed to the horizontal movement frame. The vertical movements of the scanning stage are specified in the outer while loop and the inner while loop contains both the horizontal movements and a data acquisition sub VI. Thus, with each iteration of vertical movement, the LabVIEW program will control the scanning stage to loop through all the predefined horizontal points and control the DAQ card to acquire the acoustic signals while the movements are

paused. The data collection sub VI is shown in Figure 15. The data collection section contains one for loop defined by the number of averages input from the front panel. The vertical iteration point, the horizontal iteration point, and the average loop iteration point are used inside of the for loop to determine the name sequence of the exporting '.txt' file.

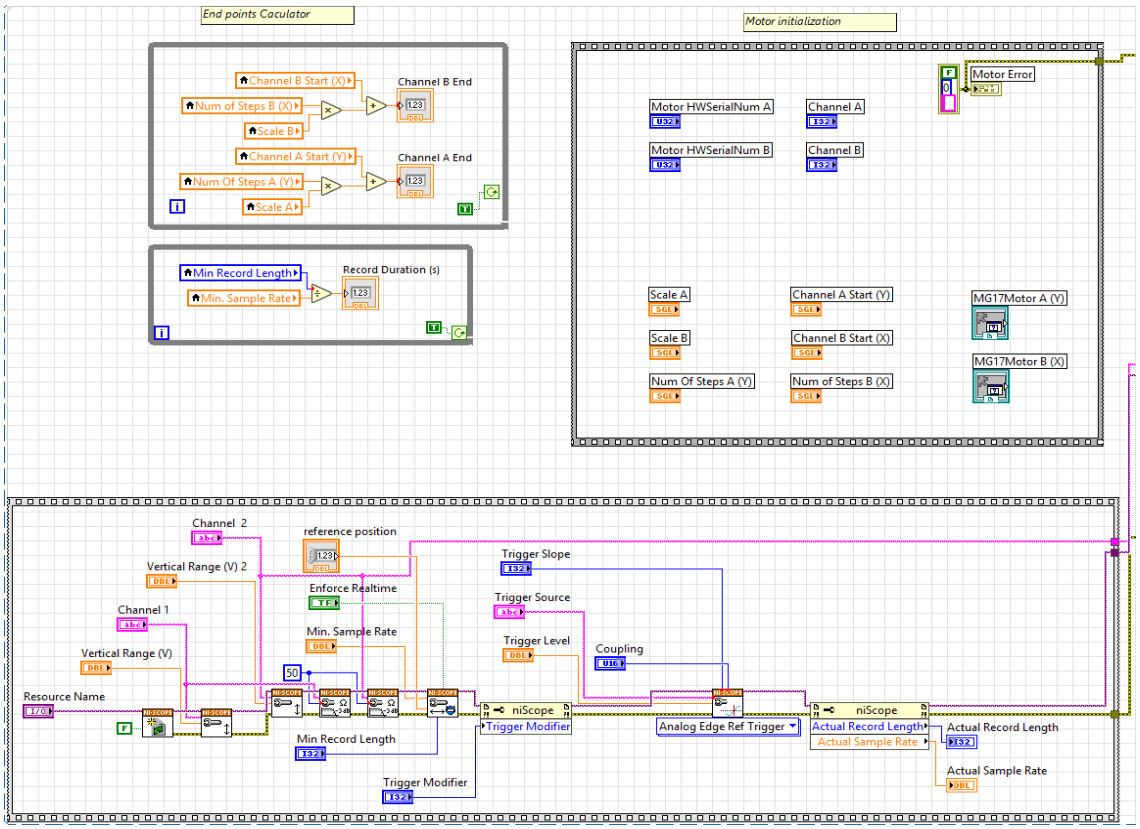

Figure 13. LabVIEW program diagram for pNDT (DAQ and motor synchronization)

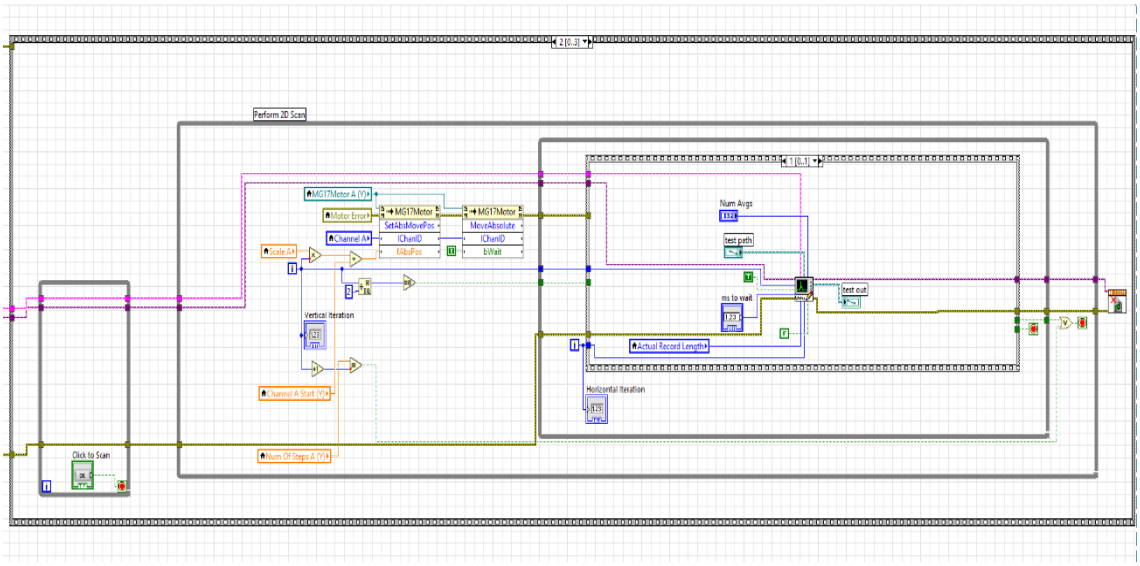

Figure 12. LabVIEW program diagram for pNDT (DAQ and motor synchronization)

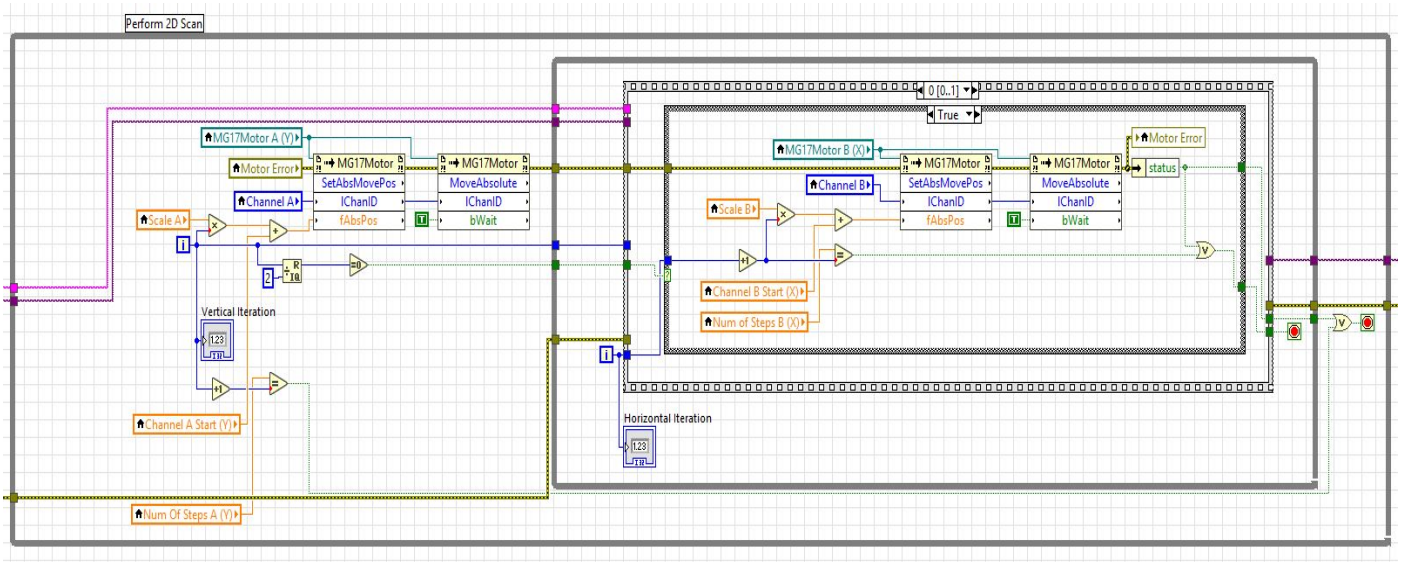

Figure 15. Nested movement-control while loops

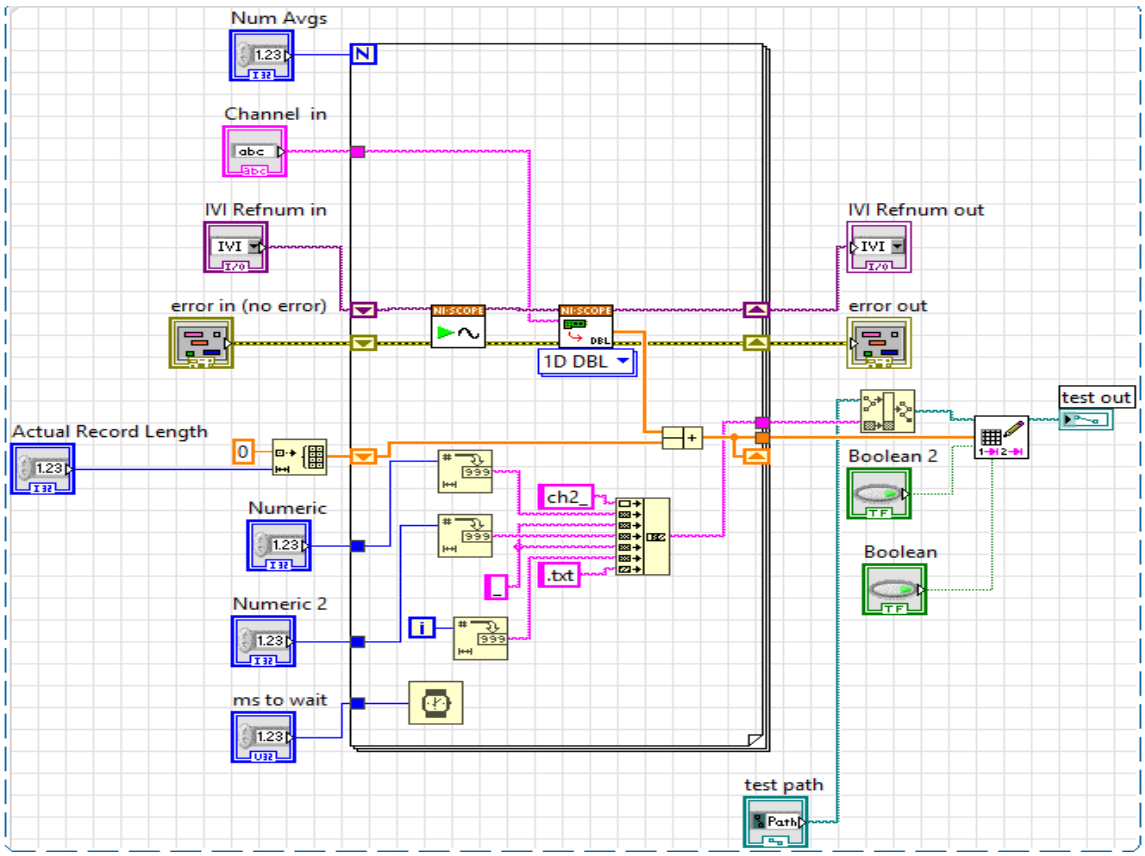

Figure 14. Data collection sub VI for pNDT LabVIEW program

2.3 Photoacoustic Detection of Damage Precursors in CFRP Composites

Figure 16 shows pNDT C-scan images in the X-Y plane parallel to the top surface of the composite sample at a depth of 25 µm. The values of the C-scan pixels are normalized from 0.1 to 1. The pNDT C-scan image (Figure 16a) contains detailed information on the composite's structure imperfections, including the X-shaped notches created for scanning. The structure and the orientation of the woven fabric are also visible. The individual carbon fiber yarn within the composite can be clearly observed.

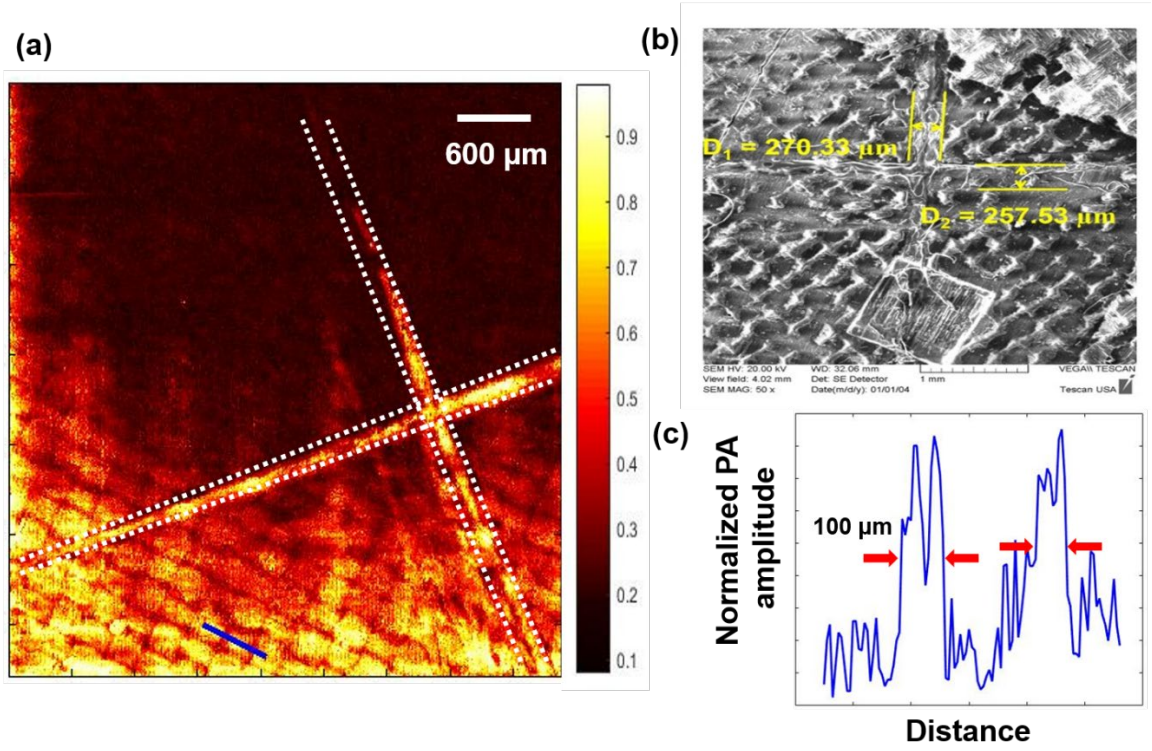

Figure 16. X-Y plane image (a) pNDT X-Y plane image (25 µm into the CFRP plate from the top surface) , the 'X' marking is highlighted, (b) SEM image, the width of the 'X' marking is calculated, (c) FWHM measurements along the blue line on the pNDT image, are taken as the lateral resolution of the image

Comparing with the scanning electron microscope (SEM) image (Figure 16b) of the same CFRP plate surface, the patterns from both images match perfectly confirming the lateral accuracy of the pNDT system. The ultrasonic signal of two grid line profiles along the blue lines in Figure 16a are extracted and shown in Figure 16c. The full width half-maximum (FWHM), 100μm, of the corresponding line spread function of the right grid line was estimated as the lateral resolution of the system at the depth of 25 μm.

Notice that the top of the C-scan image, at the depth of 25 μm, fades out to dark red color, which indicates low amplitudes of acoustic signals. This is because the surface of the CFRP plate was not perfectly orthogonal to the ultrasound transducer's focusing beam. The theory was further confirmed by projecting all C-scans into one averaged 2D x-y plane image (Figure 17). In Figure 17, the fiber yarn grids are visible across the entire imaging area, which in turn means all the surface details were captured by the 3D imaging system. While also, the crack on the back of the plate was also visible in the projected image, which proves that pNDT system has the depth penetration power to image the CFRP plate from top to bottom.

Along with x-y plane reconstructions, accurate B-scan reconstructions of the CFRP plate were created to present the defects in y-z plane (Figure 18). Figure 13a and Figure 18b show the surface notches at different positions across the plate. The B-scan results and the C-scan reconstructions obtained showed strong agreement of the defect positions, indicating that the pNDT system can reconstruct the defects of a thin CFRP plate with high accuracy.

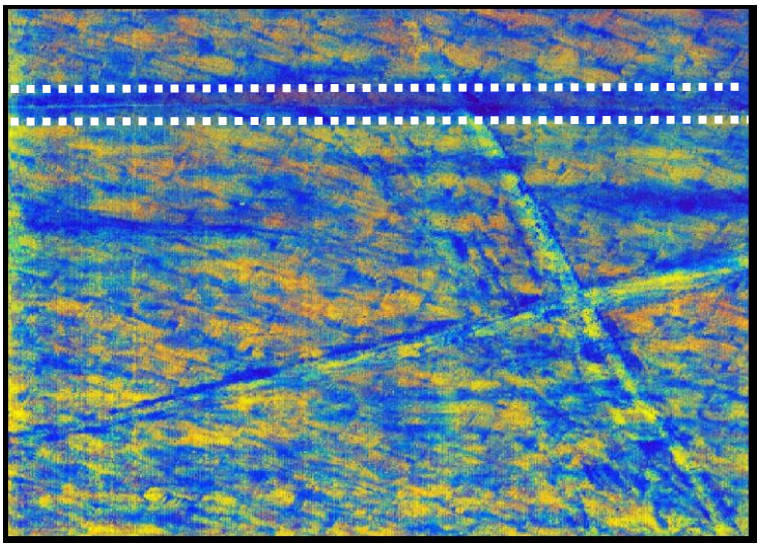

Figure 17. Average value projected X-Y plane image. Dashed white lines indicating the position of the crack that is on the back of the CFRP plate

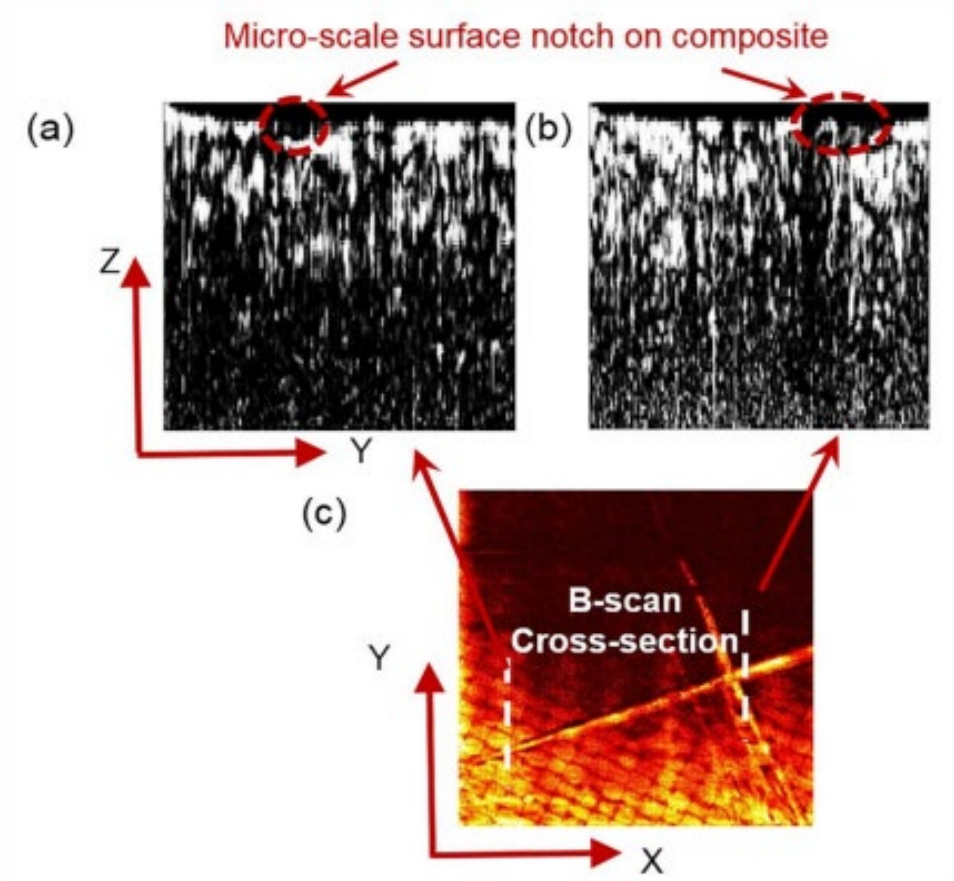

Figure 18. (a), (b) B-scan reconstruction samples of the CFRP plate. (c) X-scan image as a position reference for (a) and (b)

Chapter 3: X-ray-induced Acoustic Computed Tomography for Bone Imaging

3.1 Background

3.1.1 X-ray-induced Acoustic Computed Tomography Theory

Analogously to PA imaging, XACT effect converts the X-ray photon's energy into localized heat, which in turn generates acoustic waves proportional to the energy absorbed. During X-ray radiation, the energy is absorbed by the inner-shell electrons of the medium and photoelectrons can be generated [51], [52]. The conversion between X-ray photons and photoelectrons leads to localized temperature rise. The localized temperature rise is modeled by the heating function of XACT [7]:

$$H(r,t) = \mu_x(r)F(r,t), \qquad (8)$$

where μ_x indicates the X-ray energy absorption coefficient, and F represent the X-ray fluence function based on the location and time.

Besides the medium based absorption coefficient, pulse width of X-ray source also plays a crucial role in generation of XACT waves. A short-pulsed X-ray excitation source can be more effective in generation of acoustic waves [53]. Due to this reason, a picosecond X-ray machine was chosen for this experiment.

3.1.2 Bone Imaging Techniques

Today, bone related health issues are affecting more than 50 million adults in America [54]. Proper assessments for bone health are crucial to not only the prevention, diagnosis and monitoring of bone-related disorders, but also to serve as an indicator for other diseases symptoms [55].

Bone mineral density (BMD) imaging is one of the golden methods for determining the health of bones[56]. Among bone imaging techniques, dual-energy X-ray absorptiometry (DXA) has been the most used and thoroughly invested technology [57]. However, DXA systems can only measure the bones in two dimensions, meaning comprehensive three-dimensional (3D) microstructural information cannot be obtained. Moreover, the quality of BMD measurement by DXA degrades when imaging thick areas, as a result of the limited penetrations power of the X-ray sources used [58]. 3D bone imaging techniques have been explored by numerous scientists across the globe for replacing DXA as a better alternative. High resolution peripheral quantitative computed tomography (HR-pQCT) and modern multidetector row CT (MDCT) are two merging bone imaging modalities based on CT technology [59], [60]. However, CT based systems share the common obstacles of high dose and long operating time. Long operating time will inevitably degrade the imaging results because movements of the patients will introduce motion blur. Currently, no suitable bone imaging technique that can realize 3D imaging of bone in a short amount of time targeting the thick areas between patients' hip and spine exist. The XACT system, which utilized the spherically propagated acoustic waves, has the theoretical potentials to overcome the problems such as high dosage and long scanning time. On the grounds that the ultrasound receivers and the X-ray source can be positioned on the same side of the patients, positioning is no longer an issue and thick areas such as the hip and spine can be imaged.

In this study, the first XACT image of a chicken bone was reconstructed; plus, the detailed configurations, methods, and results will be discussed in the following sections.

3.2 Experimental Setup and Methods

3.2.1 XACT System Configuration

An XACT system configuration diagram for chicken boning imaging is shown in Figure 19**.** In the configuration, a water tank was used for coupling purposes between the ultrasound transducer and the imaged object. The chicken bone was placed on a linear adjustable stage (invisible in Figure 19) underneath the X-ray source.

After the XACT acoustic wave generation, the system can be divided into two paths: a data collection path indicated with green arrows, and a trigger detection path indicated with yellow arrows. The trigger detection path starts with a scintillator placed right beneath the water tank. When X-ray machine is firing, X-ray photons that passed through the water tank will be collected by the scintillator and converted into visible light photons. A photo diode was connected to the output of the scintillator, so that the converted photons will be detected and converted to electrical pulses. The electrical pulses were then read by a data acquisition card (NI PCI-5153EX, National Instruments) as X-ray pulsing triggers for data reconstruction. In data collection path, an ultrasound transducer with 500 KHz center frequency (NDT 902829, Olympus Panametrics) was used for receiving XACT acoustic signals. In the end, a 60 dB preamplifier (5682, Olympus) was connected between the data acquisition card and the ultrasound transducer.

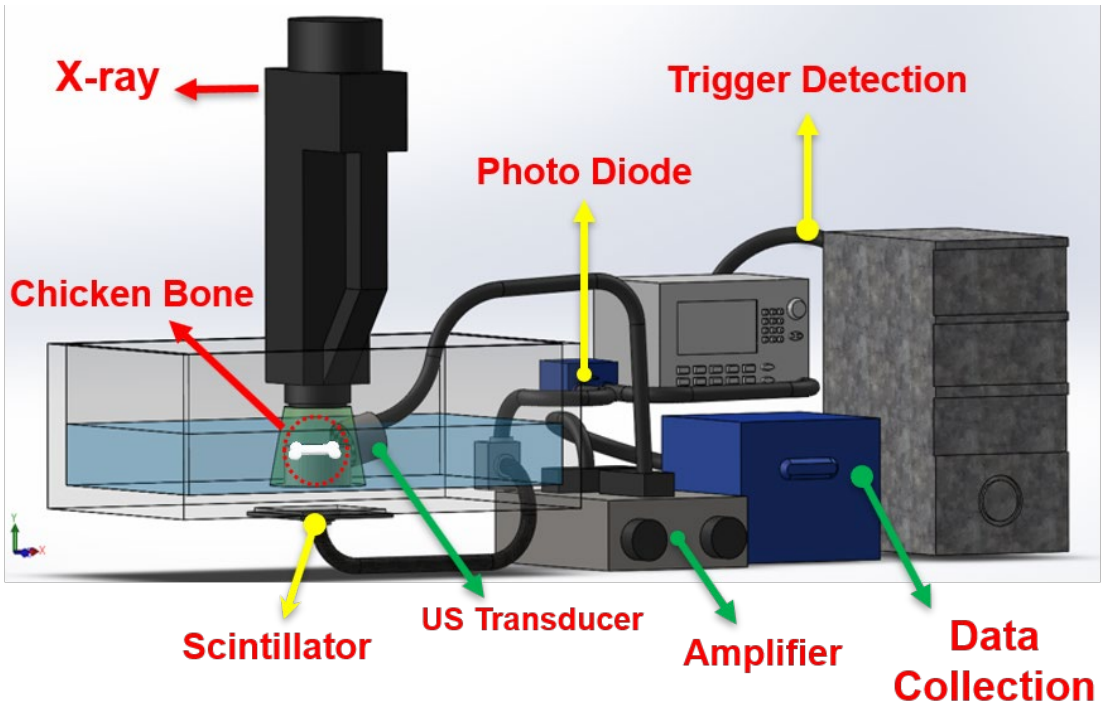

Figure 19. XACT system for single transducer scanning setup

During the scan, the linear stage holding the chicken bone sample was moved 12 times along the direction that is perpendicular to the ultrasound transducer receiving direction.

3.3 Chicken Bone Imaging Result

A preliminary image was successfully reconstructed from the chicken bone sample by back projecting the acoustic signals around the transducer locations. Figure 20 shows a comparison between a camera picture of the chicken bone and the imaging result from the XACT system. The low resolution of the resulted image is understandable, since a low-frequency ultrasound transducer was used in the experiment. Replacing the 500 KHz transducer with a high-frequency focused ultrasound transducer will improve the

axial resolution of the image. Additionally, only 12 different positions were scanned in this experiment for the reconstruction, which resulted in low lateral resolution. This can be solved by adding more steps and making the step size smaller. In future developments of the XACT system, the simple back projection reconstruction algorithm will be replaced by more sophisticated reconstructions.

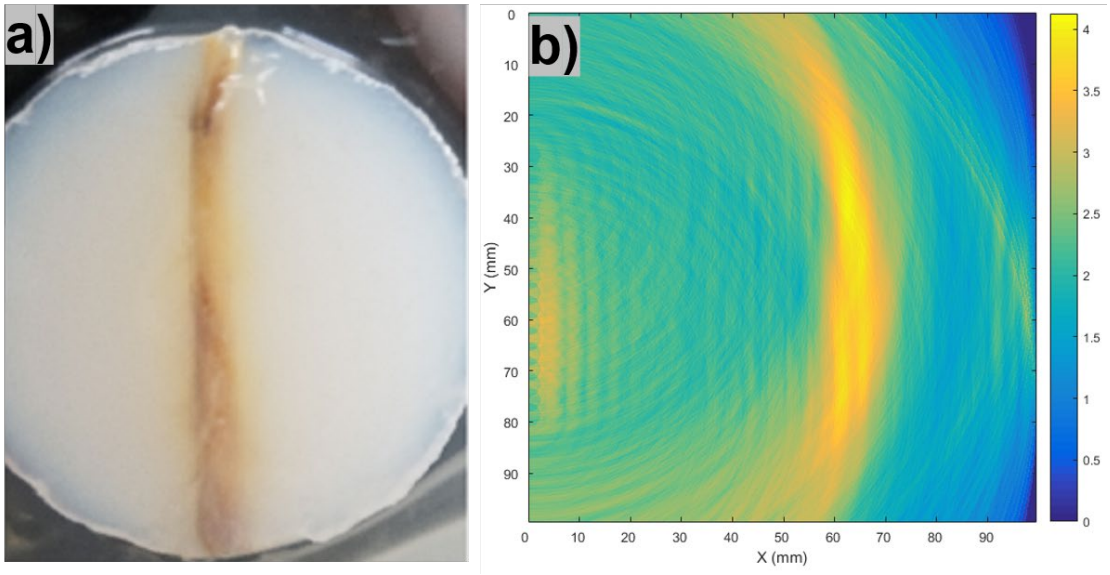

Figure 20. (a) camera picture of the chicken bone scanned; (b) reconstructed image of the chicken bone

Chapter 4: Electroacoustic Tomography to Monitor Electrical Therapy

4.1 Background

4.1.1 Electroacoustic Imaging Theory

In electroacoustic (EA) imaging, two electrodes are used as excitation source for creating high-voltage electrical field radiation. Figure 21 illustrates the EA imaging concept with a visualized electrical field. The deposited electrical energy is absorbed by a target medium, and then localized heat is generated. EA waves can then be detected because of the thermoelastic expansions. A heating function for EA wave generation is given as follows:

$$H(r,t) = \eta_E(r)A_e(r,t), \qquad (8)$$

where η_E denotes the electrical energy absorption at location r, and A_e represent the electrical energy deposition.

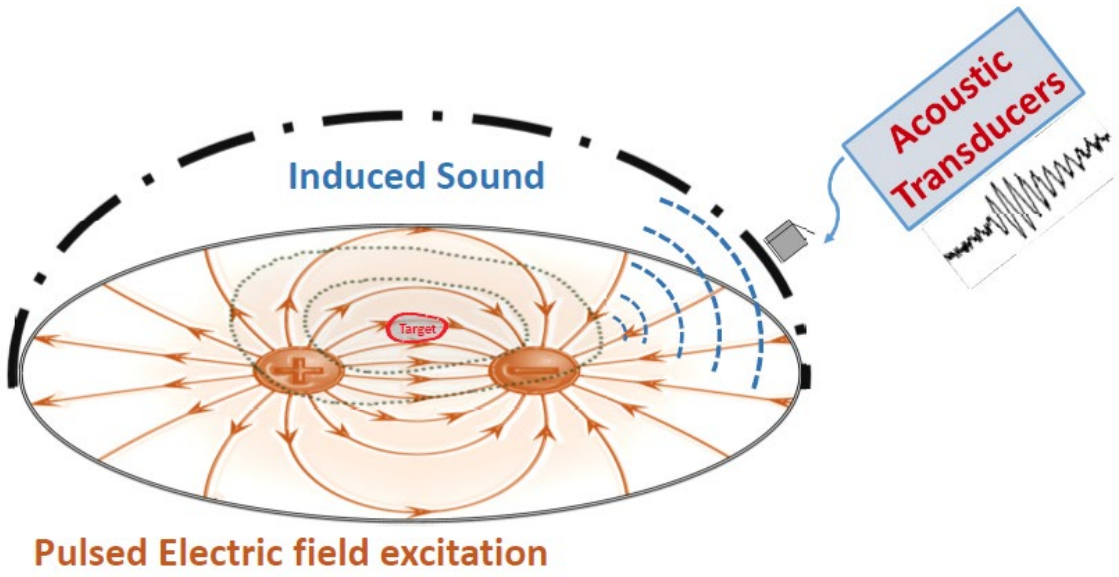

Figure 21. Schematic illustration of Electric pulse-induced Acoustic Signals

The purpose of this study is to demonstrate EAT system's capability of sensing and locating electric fields by capturing acoustic waves. Furthermore, different parameters affecting the imaging performance of EAT system are tested to better understand the characteristics of such technique.

4.1.2 Electrical Therapy Monitoring Techniques

There has been an increasing amount of electrical therapies used in clinics, i.e. cancer ablation [61]. These techniques apply high-voltage short-pulsed electricity to increase patients' cell membrane permeability. With increased membrane permeability, non-permanent drugs and genes can gain access to the inside of the cells. However, electrical therapies are often non-irreversible and location specific. So, high precision of application is required during the procedures. Currently, only monitoring systems for pre-treatment planning and post-stimulation monitoring exist, such as confocal microscopy [62], magnetic resonance imaging (MRI) [63],ultrasound imaging (US) [64], electrical impedance tomography (EIT) [65], and magnetic resonance EIT (MREIT) [66], [67]. An *in situ* monitoring technique to real-time monitor the electrical therapy procedure is invaluable.

Electroacoustic Tomography (EAT) system is developed for monitoring of such therapies by real-time imaging of the electrical field generated by the therapy electrodes. By utilizing electroacoustic (EA) waves, transducers on the outside of patient's body can capture the electric field information at procedure location and reconstruct such information to real-time monitor the electrical field changes in side patients' body.

In this study, a prototype structure of EAT system has been built. The electrical therapy procedure is simulated by two electrodes connected to a custom built high-voltage electric field generating circuit board. Acoustic signals have been captured to demonstrate the feasibility of EAT system.

4.2 Experimental Setup and Methods

4.2.1 EAT System

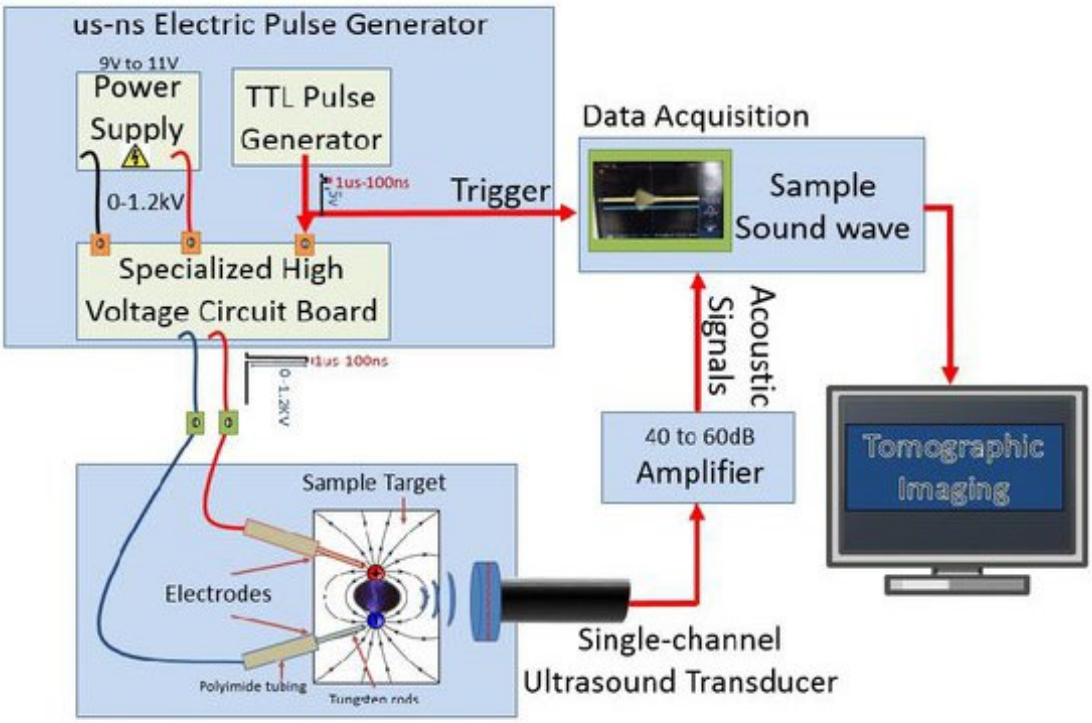

Figure 22. EAT imaging system configuration diagram

Figure 22 shows the system diagram of a developed EAT system prototype. This prototype of EAT system is designed to demonstrate the potential of sensing electrical fields by capturing EA waves using an ultrasound transducer. In order to simulate the high-voltage short-pulsed electrical therapies used in clinic, a DC to DC voltage converter

(C12 XPPOWER) is used for suppling high DC voltage to a custom built specialized high-voltage pulse generating circuit board. Two electrodes are connected to the pulse generating board and either placed in water or inserted in a tissue mimicking phantom. An ultrasound transducer is placed on the other side of the tissue mimicking phantom for acoustic wave capture. After going through a 60 dB amplifier (5682, Olympus), the acoustic signal can then be acquired by a computer mounted data acquisition card (NI PCI-5153EX, National Instruments). In order to demonstrate the performance of built EA imaging prototype, two different ultrasound transducers have been tested under different magnitudes of electrical field voltages.

4.3 Experimental Results

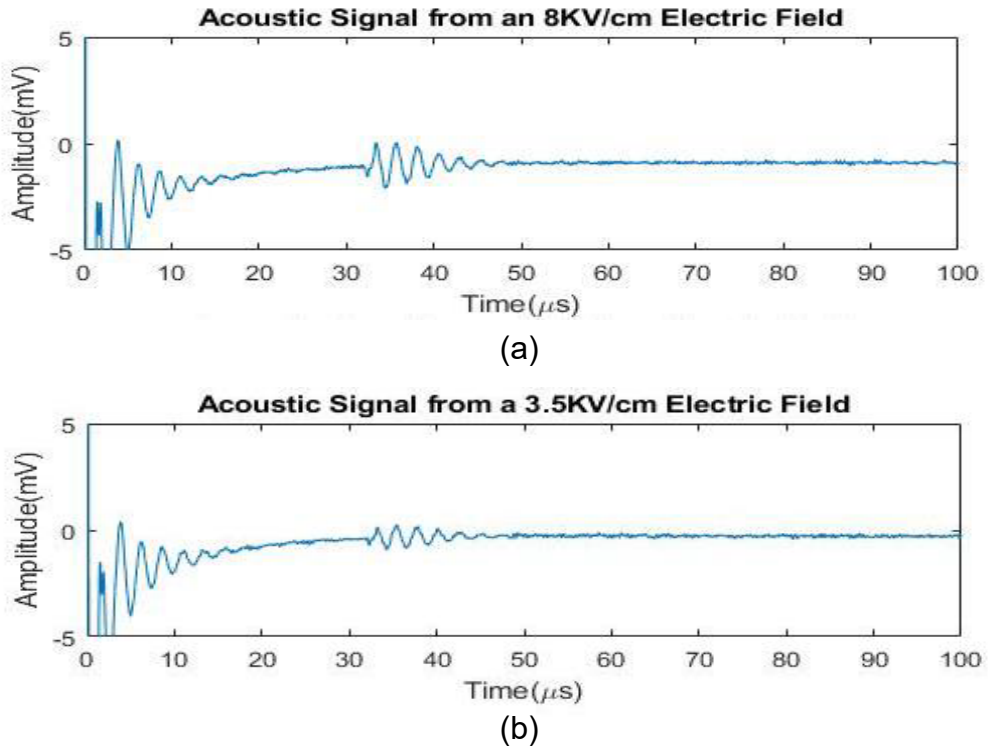

Figure 23. (a, b): Electroacoustic (EA) signals in different electric field intensity of 4.8 kV/cm, and 8 kV/cm, at 1μs pulse width, $d1 = 0.150\ cm$, $d2 = 0.340\ cm$

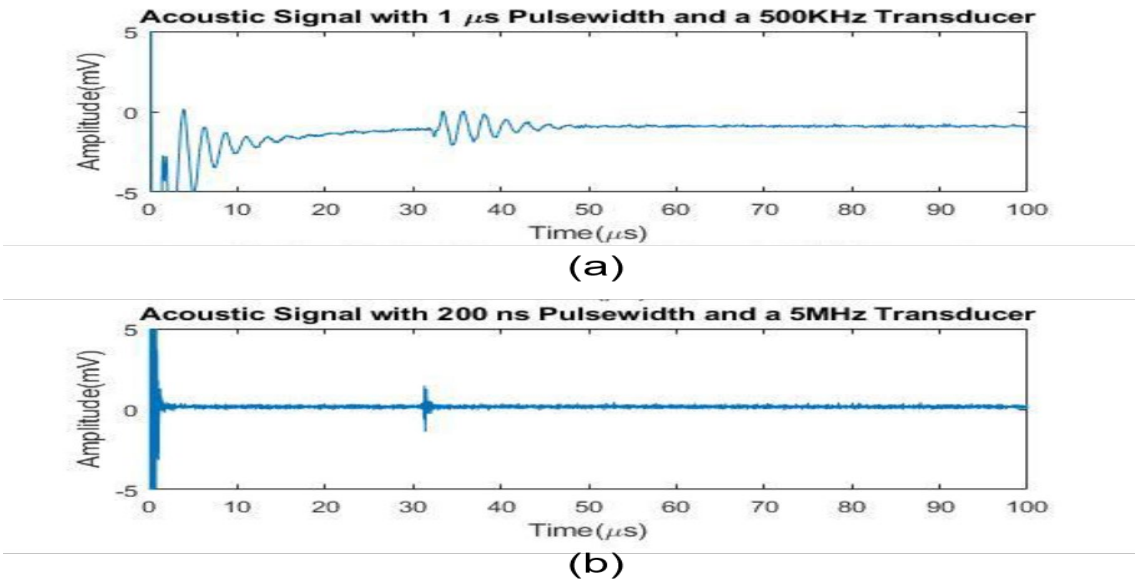

Figure 24. (a, b): Different pulse width (1 µs and 200 ns) electroacoustic (EA) signals captured by matching center frequency (500 KHz and 5 MHz) transducers in tissue mimicking phantoms

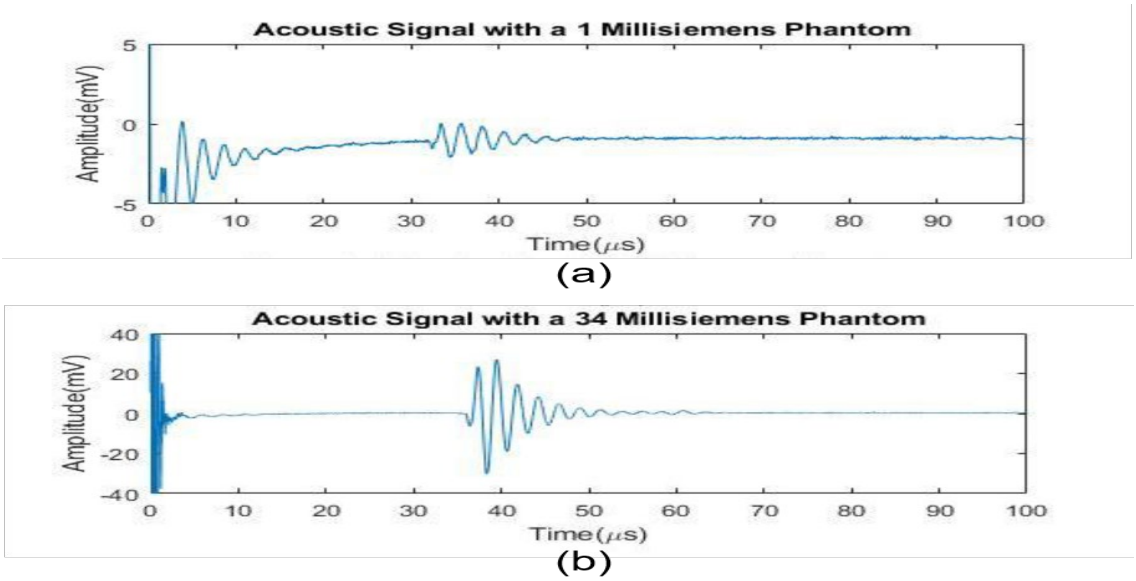

Figure 25. (a), (b): EA signal in an agar-based homogeneous phantom, transducers at Δt = 1000 ns and (a) with conductivity of 1 mS/cm, and (b) 34 mS/cm, at EF = 8 kV/cm.

In figure 23, two EA signals were captured by the same ultrasound transducer, but under different electric field intensities, 4.8 kV/cm and 8 kV/cm respectively. As demonstrated in the plots, the amplitudes of the generated acoustic signals are positively proportional to the intensity of the electric field. After comparing the effects of different electrical field strengths, different electrical field pulse -widths are also compared. Figure 24 shows the plot comparison between the generated acoustic waves from an electrical field with 1 μs pulse width and 200 ns pulse width. From the plot, the axial resolution of the test with shorter electrical field pulse width is shown to be much higher than the resolution of the longer pulse width; although, the signal-to-noise (SNR) ratio looks comparable. The higher SNR is expected on longer electrical field pulse width scenarios, when a high acoustic attenuation medium is present. The attenuation of the acoustic signals is inversely proportional to the frequency of the waves. Lastly, different conductivities of the tissue mimicking phantom are tested with the same electrical field intensity at 8 kV/cm. In figure 25, the phantom with higher conductivity (34 milli siemens) returned much higher SNR EA signals.

Chapter 5: Discussion and Conclusion

5.1 Discussion and future works

5.1.1 pNDT Discussion and Future Works

Detection sensitivity is the main criteria when evaluating pNDT system's performance. The theoretical model indicates that the resultant PA waves' amplitude is proportional to the time derivative of the excitation pulse [68]. To simplify, the pulse width of the excitation source is PA is crucial to the effective generation of acoustic waves. The implementation of the 7-picosecond pulsed laser should result in a high conversion coefficient between the light and the acoustic waves.

The laser resolution of pNDT system is given by the diffraction-limited spot size of the optical focus [47]. When the 532 nm wavelength laser source is combined with the 0.10 numerical aperture (NA) objective lens, the theoretical later resolution of pNDT is 2.7 μm, which is enough to resolve the individual carbon fibers (diameter of 5~10 μm) embedded in the CFRP plate. If the penetration depth is prioritized, the lateral resolution can be scaled down accordingly by either increasing the NA number of the objective lens or using a shorter expiation wavelength. The axial resolution of pNDT is jointly determined by the pulse width of the laser source along with the center frequency of the transducer used. If a higher frequency transducer were used, higher axial resolution can be achieved.

The demonstrated pNDT scanning speed is limited by the single ultrasonic probe for signal collection during the scanning. However, a pair of galvanometer mirrors with optical scanning can dramatically improve the imaging speed (up to 30 kHz, the limitation of a galvanometer) and will be faster than any mechanical-scanning imaging system. Additionally,

by increasing the repetition rate of the excitation laser, the speed of the pNDT system can be further improved.

5.1.2 XACT system Discussion and Future Works

XACT is a novel imaging modality that has the potential to allow 3D reconstruction of bone structure with a single projection of X-ray. It also theoretically deposits lower dose in patients as compared to conventional CT based techniques. Furthermore, with powerful enough data processing equipment, real-time 3D bone imaging is achievable.

The first XACT system bone imaging was reconstructed in this study, which is significant to prove the bone imaging potential of the XACT system. For the future development of the XACT system, a cup-shaped ultrasound transducer array can replace the single ultrasound transducer to enable the 3D imaging capability (Figure 26). An ultrasound cup detector has ultrasound transducer elements mounted on the inside of the cup surface. By utilizing the spherically propagated XA waves, a 3D reconstruction can be realized with one projection of X-ray.

A 72-channel cup-shaped ultrasound probe is already being tested for such a job. In addition to the multi-channel ultrasound probe, a 128-channel pre-amplifier and a 128-channel data acquisition machine have already been tested and are ready to be implemented into the next generation XACT system for single pulsed 3D bone imaging. The next step is to develop and implement the cup ultrasound transducer array reconstruction algorithm to demonstrate the 3D imaging capability of XACT. Total dose

from a single X-ray projection can be verified after obtaining the image by using an ion chamber to confirm the claimed low-dose character of XACT.

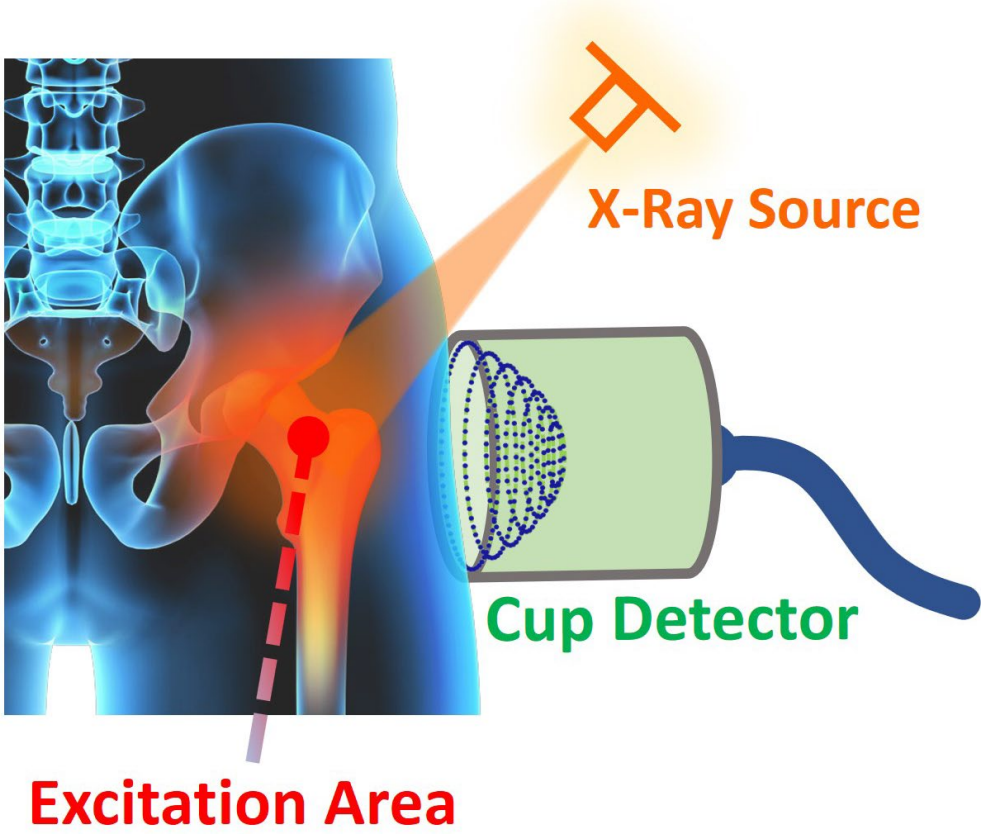

Figure 26. the next generation single projection 3D bone imaging concept of XACT system with an ultrasound cup detector

5.1.3 EAT system Discussion and Future Works

In this study, the acoustic signals generated by high-voltage pulsing electrical fields were detected and analyzed. The optimal parameters for effective EA signal generating were found. Based on a theoretical model and experimental testing, the duration of the electric pulse, the intensity of the electric field, and the conductivity of the stimulating medium all effect the generation of the acoustic waves. The study indicates that acoustic pressure waves can monitor electrotherapy in the range of μs-ns electric pulse duration. The present experimental results further validate the principle of real-time

monitoring of electric-field excitation as a new technique for clinical electrotherapy applications.

With the verification of acoustic signals from pulsing electric fields in water and phantom, a more robust and static-electricity proof polychlorinated biphenyl (PCB) design has been created for the high-voltage electric field generating circuit. The design of the printed circuit board (PCB) is shown in Figure 27, and the 3D realization of the PCB in Autodesk Fusion 360 [69] is shown in Figure 28. The PCB manufacturing of the board will allow the circuit to be housed inside of a portable chassis, which in term will greatly enhance the portability of the EAT system.

For the future development of EAT system for monitoring electric therapies, the high-voltage pulsing circuit can be upgraded to provide high-voltage pulses with overall higher wattage design. A new DC-to-DC boost convert chip, XP POWER F50, will allow a design of 5000 Volts pulsing electric field with a total power consumption of 10 Watts.

Besides upgrading the electric field generating circuit, an ultrasound ring-array will be replacing the single transducer for the detection of acoustic waves. With the addition of a ring array, monitoring the dynamics of electric fields become a possibility. The challenges remain to be finding out ways to improve the SNR of received acoustic signals. The solution can be designing a better amplification stage or improving the reconstruction algorithms.

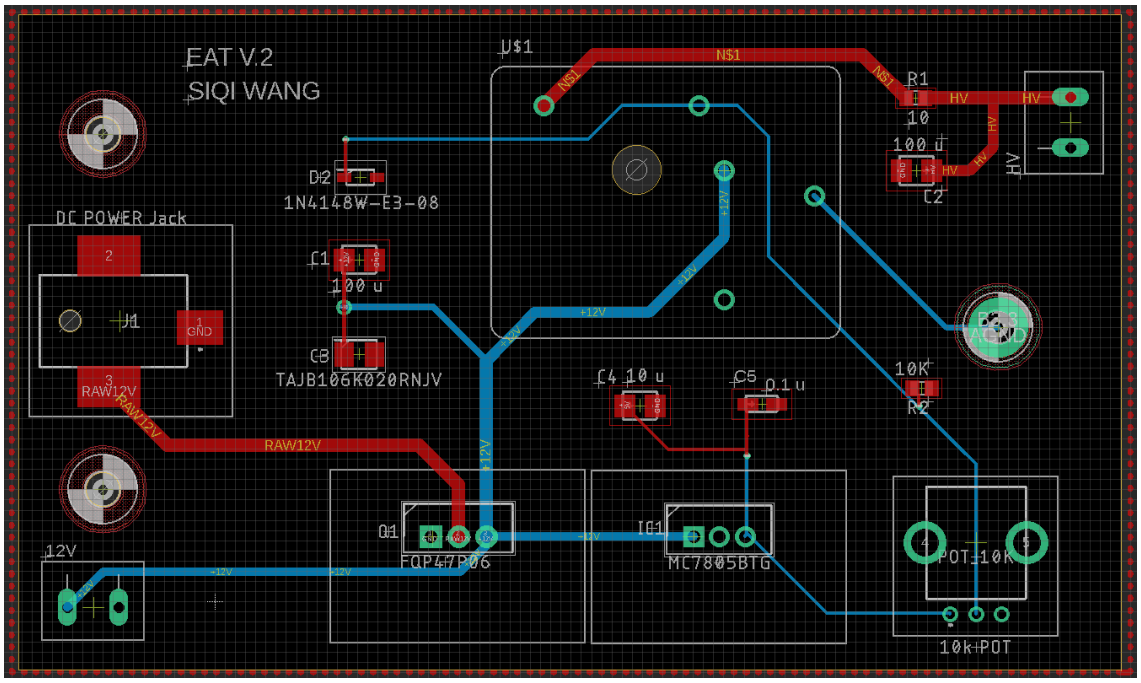

Figure 27. PCB design for EAT high-voltage electric field generating circuit

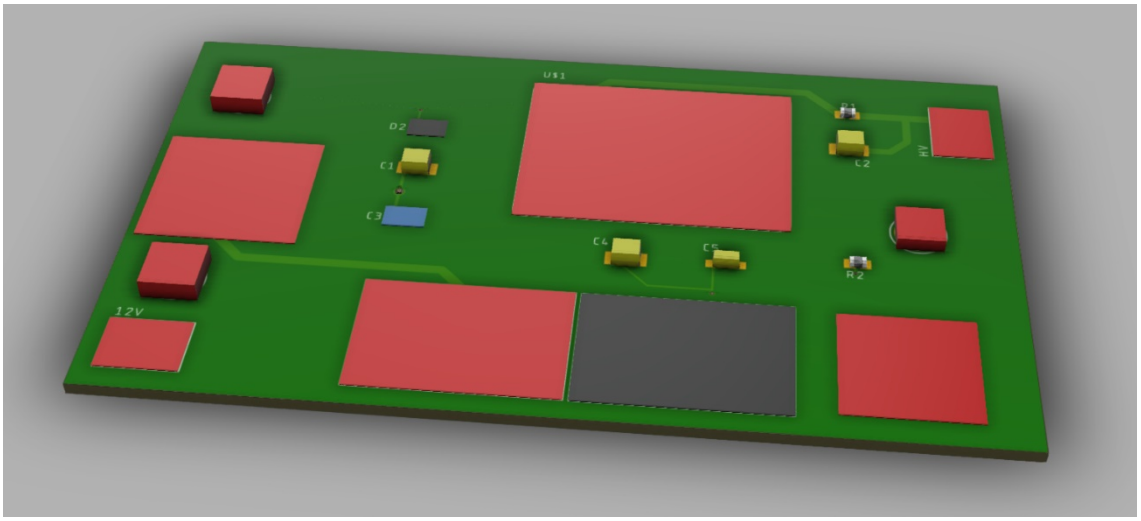

Figure 28. 3D realization of the PCB design

5.2 Conclusion

With inherent hybrid waveform nature, radiation-induced acoustic imaging techniques offer multiple advantages over the conventional pure radiation based or pure sound based imaging modalities. The combination of radiation high contrast and acoustic-diffraction-limited spatial resolution associated with low scattering of ultrasonic waves makes radiation-induced acoustic imaging techniques particularly suitable for biomedical and non-destructive testing purposes.

The development progress of multiple novel radiation-induced acoustic imaging modalities, utilizing photoacoustic (PA) effect, X-ray-induced acoustic (XA) effect and electroacoustic (EA) effect, has been report in this study.

Overall, the radiation-induced acoustic imaging systems are still in their 'infancy'. Improvements in terms of sensitivity, speed, and ease of use still need to be made. Many design obstacles, including, but not limited to reconstruction algorithm optimization, must be conquered before they can be applied to the practical fields.

References

[1] A. G. Bell, "On the production and reproduction of sound by light," *Am J Sci*, vol. Series 3 Vol. 20, no. 118, pp. 305–324, Oct. 1880.

[2] A. A. Karabutov, N. B. Podymova, and V. S. Letokhov, "Time-resolved laser optoacoustic tomography of inhomogeneous media," 1996. p. 19

[3] R. A. Kruger, P. Liu, Y. "Richard" Fang, and C. R. Appledorn, "Photoacoustic ultrasound (PAUS)—Reconstruction tomography," *Medical Physics*, vol. 22, no. 10, pp. 1605–1609, 1995.

[4] L. V. Wang, "Tutorial on Photoacoustic Microscopy and Computed Tomography," *IEEE Journal of Selected Topics in Quantum Electronics*, vol. 14, no. 1, pp. 171–179, Jan. 2008.

[5] T. Bowen, "Radiation-Induced Thermoacoustic Soft Tissue Imaging," in *1981 Ultrasonics Symposium*, 1981, pp. 817–822.

[6] A. Zarafshani, J. Merrill, S. Wang, B. Zheng, and L. Xiang, "Electroacoustic tomography system with nanosecond electric pulse excitation source," in *Medical Imaging 2019: Ultrasonic Imaging and Tomography*, 2019, vol. 10955, p. 109551B.

[7] S. Liu, R. Zhang, Z. Zheng, and Y. Zheng, "Electromagnetic–Acoustic Sensing for Biomedical Applications," *Sensors (Basel)*, vol. 18, no. 10, Sep. 2018.

[8] J. Xia, J. Yao, and L. V. Wang, "Photoacoustic tomography: principles and advances," *Electromagn Waves (Camb)*, vol. 147, pp. 1–22, 2014.

[9] V. E. Gusev and A. A. Karabutov, "Laser optoacoustics," *NASA STI/Recon Technical Report A*, vol. 93, Jul. 1991.

[10] P. M. Morse, H. Feshbach, and E. U. Condon, "Methods of Theoretical Physics Parts I & II," *Physics Today*, vol. 7, no. 12, p. 15, Jan. 2009.

[11] L. E. Kinsler, A. R. Frey, A. B. Coppens, and J. V. Sanders, *Fundamentals of Acoustics, 4th Edition*. 1999.

[12] S. L. Jacques, "Optical properties of biological tissues: a review," *Phys. Med. Biol.*, vol. 58, no. 11, pp. R37–R61, May 2013.

[13] A. L. Robinson, "Imaging unaltered cell structures with x-rays," *Science*, vol. 237, no. 4816, pp. 723–724, Aug. 1987.

[14] A. L. Robinson, "High-resolution imaging with soft x-rays," *Science*, vol. 215, no. 4529, pp. 150–152, Jan. 1982.

[15] R. Neutze, R. Wouts, D. van der Spoel, E. Weckert, and J. Hajdu, "Potential for biomolecular imaging with femtosecond X-ray pulses," *Nature*, vol. 406, no. 6797, p. 752, Aug. 2000.

[16] M. Dierolf *et al.*, "Ptychographic X-ray computed tomography at the nanoscale," *Nature*, vol. 467, no. 7314, pp. 436–439, Sep. 2010.

[17] A. Berrington de González *et al.*, "Projected cancer risks from computed tomographic scans performed in the United States in 2007," *Arch. Intern. Med.*, vol. 169, no. 22, pp. 2071–2077, Dec. 2009.

[18] L. Xiang, B. Han, C. Carpenter, G. Pratx, Y. Kuang, and L. Xing, "X-ray acoustic computed tomography with pulsed x-ray beam from a medical linear accelerator," *Med Phys*, vol. 40, no. 1, Jan. 2013.

[19] J. Kim *et al.*, "X-Ray Acoustic-Based Dosimetry Using a Focused Ultrasound Transducer and a Medical Linear Accelerator," *IEEE Transactions on Radiation and Plasma Medical Sciences*, vol. 1, no. 6, pp. 534–540, Nov. 2017.
[20] and, and, and, and, and and, "Broadband detection of dynamic acoustic emission process induced by 6 MV therapeutic X-ray beam from a clinical linear accelerator," in *2015 IEEE International Ultrasonics Symposium (IUS)*, 2015, pp. 1–4.
[21] D. R. T. Sampaio, J. H. Uliana, A. A. O. Carneiro, J. F. Pavoni, T. Z. Pavan, and L. F. Borges, "X-ray acoustic imaging for external beam radiation therapy dosimetry using a commercial ultrasound scanner," in *2015 IEEE International Ultrasonics Symposium (IUS)*, 2015, pp. 1–4.
[22] S. Tang *et al.*, "X-ray-induced acoustic computed tomography with an ultrasound transducer ring-array," *Appl. Phys. Lett.*, vol. 110, no. 10, p. 103504, Mar. 2017.
[23] M. Hossain and M. Su, "Nanoparticle location and material dependent dose enhancement in X-ray radiation therapy," *J Phys Chem C Nanomater Interfaces*, vol. 116, no. 43, pp. 23047–23052, Nov. 2012.
[24] G. J. Hine and G. L. Brownell, *Radiation Dosimetry*. Elsevier, 2013.
[25] B. Mijnheer, S. Beddar, J. Izewska, and C. Reft, "In vivo dosimetry in external beam radiotherapy," *Med Phys*, vol. 40, no. 7, p. 070903, Jul. 2013.
[26] S. Hickling, M. Hobson, and I. E. Naqa, "Feasibility of X-Ray Acoustic Computed Tomography as a Tool for Noninvasive Volumetric In Vivo Dosimetry," *International Journal of Radiation Oncology • Biology • Physics*, vol. 90, no. 1, p. S843, Sep. 2014.
[27] S. Hickling, H. Lei, M. Hobson, P. Léger, X. Wang, and I. E. Naqa, "Experimental evaluation of x-ray acoustic computed tomography for radiotherapy dosimetry applications," *Medical Physics*, vol. 44, no. 2, pp. 608–617, 2017.
[28] P. E. Mix, *Introduction to Nondestructive Testing: A Training Guide*. John Wiley & Sons, 2005.
[29] L. Cartz, *Nondestructive testing: radiography, ultrasonics, liquid penetrant, magnetic particle, eddy current*. ASM International, 1995.
[30] A. S. M. International, *Asm Handbook: Nondestructive Evaluation and Quality Control*. ASM International, 1989.
[31] S. Gholizadeh, "A review of non-destructive testing methods of composite materials," *Procedia Structural Integrity*, vol. 1, pp. 50–57, Jan. 2016.
[32] J. Hoła and K. Schabowicz, "State-of-the-art non-destructive methods for diagnostic testing of building structures – anticipated development trends," *Archives of Civil and Mechanical Engineering*, vol. 10, no. 3, pp. 5–18, Jan. 2010.
[33] S. Tang, C. Ramseyer, P. Samant, and L. Xiang, "X-ray-induced acoustic computed tomography of concrete infrastructure," *Appl. Phys. Lett.*, vol. 112, no. 6, p. 063504, Feb. 2018.
[34] I. Pelivanov *et al.*, "High resolution imaging of impacted CFRP composites with a fiber-optic laser-ultrasound scanner," *Photoacoustics*, vol. 4, no. 2, pp. 55–64, Jun. 2016.
[35] National Instrument, *Laboratory Virtual Instrument Engineering Workbench (LabVIEW)*. .

[36] U. Meier, “Carbon Fiber-Reinforced Polymers: Modern Materials in Bridge Engineering,” *Structural Engineering International*, vol. 2, no. 1, pp. 7–12, Feb. 1992.
[37] W. J. Cantwell and J. Morton, “The impact resistance of composite materials — a review,” *Composites*, vol. 22, no. 5, pp. 347–362, Sep. 1991.
[38] P. Schemmel and A. J. Moore, “Monitoring stress changes in carbon fiber reinforced polymer composites with GHz radiation,” *Appl Opt*, vol. 56, no. 22, pp. 6405–6409, Aug. 2017.
[39] G. Tsigkourakos, V. V. Silberschmidt, and I. A. Ashcroft, “Damage assessment in CFRP laminates exposed to impact fatigue loading,” *J. Phys.: Conf. Ser.*, vol. 305, p. 012047, Jul. 2011.
[40] S. A. Michel, R. Kieselbach, and H. J. Martens, “Fatigue strength of carbon fibre composites up to the gigacycle regime (gigacycle-composites),” *International Journal of Fatigue*, vol. 28, no. 3, pp. 261–270, Mar. 2006.
[41] W. J. Cantwell and J. Morton, “Detection of impact damage in CFRP laminates,” *Composite Structures*, vol. 3, no. 3, pp. 241–257, Jan. 1985.
[42] J. Zhang *et al.*, “Nondestructive Evaluation of Carbon Fiber Reinforced Polymer Composites Using Reflective Terahertz Imaging,” *Sensors*, vol. 16, no. 6, p. 875, Jun. 2016.
[43] C. Goidescu *et al.*, “Damage investigation in CFRP composites using full-field measurement techniques: Combination of digital image stereo-correlation, infrared thermography and X-ray tomography,” *Composites Part B: Engineering*, vol. 48, pp. 95–105, May 2013.
[44] Y. H. Wong, R. L. Thomas, and G. F. Hawkins, “Surface and subsurface structure of solids by laser photoacoustic spectroscopy,” *Appl. Phys. Lett.*, vol. 32, no. 9, pp. 538–539, May 1978.
[45] J. J. Pouch, R. L. Thomas, Y. H. Wong, J. Schuldies, and J. Srinivasan, “Scanning photoacoustic microscopy for nondestructive evaluation,” *J. Opt. Soc. Am., JOSA*, vol. 70, no. 5, pp. 562–564, May 1980.
[46] T. Hoshimiya, H. Endoh, and Y. Hiwatashi, “NDE of a subsurface defect in a magnetic disk head and surface defects fabricated on metal plate by photoacoustic microscopy,” in *1996 IEEE Ultrasonics Symposium. Proceedings*, 1996, vol. 2, pp. 789–792 vol.2.
[47] Y. Zhou, J. Yao, and L. V. Wang, “Tutorial on photoacoustic tomography,” *J Biomed Opt*, vol. 21, no. 6, Jun. 2016.
[48] B. E. Treeby and B. T. Cox, “k-Wave: MATLAB toolbox for the simulation and reconstruction of photoacoustic wave fields,” *JBO*, vol. 15, no. 2, p. 021314, Mar. 2010.
[49] “MATLAB - MathWorks.” [Online]. Available: https://www.mathworks.com/products/matlab.html. [Accessed: 14-Apr-2019].
[50] “APT with LabVIEW.” [Online]. Available: https://www.thorlabs.com/newgrouppage9.cfm?objectgroup_id=8348. [Accessed: 17-Apr-2019].
[51] null Garcia, null Pastor, and null Bennemann, “Theory for the photoacoustic response to x-ray absorption,” *Phys. Rev. Lett.*, vol. 61, no. 1, pp. 121–124, Jul. 1988.

[52] L. Nie, D. Xing, Q. Zhou, D. Yang, and H. Guo, "Microwave-induced thermoacoustic scanning CT for high-contrast and noninvasive breast cancer imaging," *Med Phys*, vol. 35, no. 9, pp. 4026–4032, Sep. 2008.
[53] L. Xiang, S. Tang, M. Ahmad, and L. Xing, "High Resolution X-ray-Induced Acoustic Tomography," *Scientific Reports*, vol. 6, p. 26118, May 2016.
[54] "Osteoporosis Fast Facts," *National Osteoporosis Foundation*. [Online]. Available: https://www.nof.org/news-events/pressmedia-kit/osteoporosis-fast-facts/. [Accessed: 09-Apr-2019].
[55] T. Hamaoka, J. E. Madewell, D. A. Podoloff, G. N. Hortobagyi, and N. T. Ueno, "Bone Imaging in Metastatic Breast Cancer," *Journal of Clinical Oncology*, vol. 22, no. 14, pp. 2942–2953, Jul. 2004.
[56] T. M. Link and S. Majumdar, "Osteoporosis imaging," *Radiologic Clinics*, vol. 41, no. 4, pp. 813–839, Jul. 2003.
[57] Y. J. Choi, "Dual-Energy X-Ray Absorptiometry: Beyond Bone Mineral Density Determination," *Endocrinol Metab (Seoul)*, vol. 31, no. 1, pp. 25–30, Mar. 2016.
[58] H. H. Bolotin, "DXA in vivo BMD methodology: An erroneous and misleading research and clinical gauge of bone mineral status, bone fragility, and bone remodelling," *Bone*, vol. 41, no. 1, pp. 138–154, Jul. 2007.
[59] M. Burrows, D. Liu, and H. McKay, "High-resolution peripheral QCT imaging of bone micro-structure in adolescents," *Osteoporos Int*, vol. 21, no. 3, pp. 515–520, Mar. 2010.
[60] C. Chen *et al.*, "Quantitative imaging of peripheral trabecular bone microarchitecture using MDCT," *Med Phys*, vol. 45, no. 1, pp. 236–249, Jan. 2018.
[61] L. Miller, J. Leor, and B. Rubinsky, "Cancer Cells Ablation with Irreversible Electroporation," *Technol Cancer Res Treat*, vol. 4, no. 6, pp. 699–705, Dec. 2005.
[62] R. Hemmler, G. Böse, R. Wagner, and R. Peters, "Nanopore Unitary Permeability Measured by Electrochemical and Optical Single Transporter Recording," *Biophys J*, vol. 88, no. 6, pp. 4000–4007, Jun. 2005.
[63] Y. Guo *et al.*, "Irreversible electroporation in the liver: contrast-enhanced inversion-recovery MR imaging approaches to differentiate reversibly electroporated penumbra from irreversibly electroporated ablation zones," *Radiology*, vol. 258, no. 2, pp. 461–468, Feb. 2011.
[64] E. W. Lee, C. Chen, V. E. Prieto, S. M. Dry, C. T. Loh, and S. T. Kee, "Advanced hepatic ablation technique for creating complete cell death: irreversible electroporation," *Radiology*, vol. 255, no. 2, pp. 426–433, May 2010.
[65] Y. Granot, A. Ivorra, E. Maor, and B. Rubinsky, "In vivo imaging of irreversible electroporation by means of electrical impedance tomography," *Phys Med Biol*, vol. 54, no. 16, pp. 4927–4943, Aug. 2009.
[66] M. Kranjc *et al.*, "In situ monitoring of electric field distribution in mouse tumor during electroporation," *Radiology*, vol. 274, no. 1, pp. 115–123, Jan. 2015.
[67] M. Kranjc, S. Kranjc, F. Bajd, G. Serša, I. Serša, and D. Miklavčič, "Predicting irreversible electroporation-induced tissue damage by means of magnetic resonance electrical impedance tomography," *Sci Rep*, vol. 7, no. 1, p. 10323, 04 2017.
[68] A. M. Winkler, K. Maslov, and L. V. Wang, "Noise-equivalent sensitivity of photoacoustics," *J Biomed Opt*, vol. 18, no. 9, Sep. 2013.

[69] “Fusion 360 | Free Software for Students and Educators | Autodesk.” [Online]. Available: https://www.autodesk.com/products/fusion-360/students-teachers-educators. [Accessed: 18-Apr-2019].